OPTIMIZATION OF A PULSED SOURCE-SINK

MICROSCALE MIXING DEVICE

By

Baratunde Aole Cola

Thesis

Submitted to the Faculty of the

Graduate School of Vanderbilt University

in partial fulfillment of the requirements

for the degree of

MASTER OF SCIENCE

in

Mechanical Engineering

December, 2004

Nashville, Tennessee

Approved:

Professor Mark A. Stremler

Professor Greg D. Walker

ACKNOWLEDGMENTS

TABLE OF CONTENTS

Page

Chapter

LIST OF FIGURES

Figure		Page

NOMENCLATURE

Symbol - Meaning	Symbol - Meaning
μ-TAS – miniaturized total analysis system	m – meter
DNA – deoxyribonucleic acid	A – area
x, y, z – regular Cartesian coordinates	s – seconds
: - indicates ratio	nl – nanoliter
V – velocity (or volt)	t – time
PDMS – polydimethyl siloxane	PC – personal computer
ODEs – ordinary differential equations	mm – millimeter
3-D – three dimensional	MM – microfluidic module
2-D – two dimensional	μm – micrometer
MEMS – micro mechanical electrical system	μl – microliter
PSSMD – pulsed source-sink mixing device	cm – centimeter
Re – Reynolds number	I/O – input/output
q – source-sink strength, or flow rate	" – inch
sn(z,k) – Jacobian elliptic sine	ml – milliliter
K(k) – complete elliptic integral of the 1st kind	Z – complex coordinate
L – length	CAD – computer-aided design
p – period	σ - Lyapunov exponent
u – x component of velocity	Ψ - stream function
v – y component of velocity, or viscosity	D – diameter
w – z component of velocity	VI – virtual instrument

CHAPTER I

INTRODUCTION

Overview

The mixing of fluids is intimately involved in the workings of the world, from the large scale mixing that occurs in the mantle of the earth to the small scale mixing that occurs in the blood vessels of the human body [1]. Improving the ability to mix things has long been a concern of advancing society. As the 21st century is championed in, and with it a new era of technology, the need for novel mixing technologies continues to increase. In this study, the fundamentals of chaotic advection are leveraged to analyze and test a mixing application. Chaotic advection is directly related to mixing through its ability to create stirring, or highly stretched particle interfaces, in a fluid, which in turn promotes enhanced mixing by increasing the area over which high concentrations in a flow can molecularly diffuse to lower concentrations.

One of the greatest advancing trends of today's modern society is its ability to view, study, and create in the world on smaller and smaller scales. The hot topic of the 1980's and 1990's was micro-level sciences, now it is nano-level sciences. As the ability to manipulate objects expands into smaller and smaller scales, the challenge presented to fluid scientists is to find new ways to mix at these levels.

A common result of having small length scales in a system, as in the case of microfluidic devices, is having low Reynolds number fluid flow [2, 3, 4]. Low Reynolds number flow, or laminar flow, is traditionally associated with poor mixing. This phenomenon is made clear when one closely examines the nature of laminar flow. From

a Eulerian point of view, the governing equations for the velocity field in laminar flow are linear in nature and therefore no chaos can be found. In a more physical example, looking at a fluid from the Lagrangian point of view, in laminar flow a fluid particle travels along the regular, nonintersecting streamlines of the flow. Because of this streamline motion there is no chaos or interfacial stretching between any two fluid particles in a laminar flow (the exception being chaotically advected flow as will be explained in the background of this chapter). Aref's unveiling of the idea of 'chaotic advection' [5], as explained in the background of this chapter, changed the way mixing in laminar flow is viewed. Aref was able to show that in some spatial-temporal arrangements of laminar flow chaos, or enhanced interfacial stretching, can be induced, resulting in the promotion of good mixing. Chaotic advection has opened the door to several possible mixing applications involving laminar flow; the most exciting of these applications are related to microfluidic biological and chemical systems [6 – 13], where the flow regime is usually laminar [30].

The first microfluidic device emerged in the literature in 1979 [14]. The interest in microfluidic devices was rather stagnant over subsequent years until the early 1990's, when the concept of the Miniaturized Total Chemical Analysis System (μ-TAS) was proposed [15]. This system has found a home in the fields of gene expression profiling, drug discovery, disease diagnosis, toxicology, environmental biotechnology, and forensics [16 – 24]. The miniature scale total analysis system boasted benefits of increased portability, decreased analyte consumption, shorter assay duration, and decreased cost in fabrication, implementation, and disposal. This concept turned the heads of the scientific community, promising to revolutionize the state of modern

medicine, and directed a lot of attention towards microfluidics. Since the microfluidic 'boom', many mixing applications have been proposed that leverage microscale flow science. A piece in the literature entitled *Designing for chaos: Applications of chaotic advection at the microscale* [3], provides an excellent catalogue of key microscale mixing devices that have been suggested over the years.

The development of the μ-TAS and its applicability to DNA hybridization is a root motivator of this study. DNA hybridization is governed by the tendency of nucleotide base pairs to combine with their complements. This natural propensity has become an important element of biological discovery. The biological tool of DNA microarray analysis is used widely in genomic research [25]. The success of this tool depends largely on having DNA molecules, suspended in a small fluid volume (about 0.05 ml) with a large aspect ratio (about 2000:1), uniformly sample as much of the surface as possible [25]. During standard use, molecular diffusion of the DNA is the sole mode of transport and thus requires very long sampling times and high concentrations of DNA. These requirements greatly limit the potential of this technology. Imposing a flow on the hybridization solution has been proposed as a means of overcoming the limitations on this diffusion-limited sensing and has been observed to increase the sensitivity of the process [26]. Imposing a flow provides for more rapid and more uniform target delivery [27, 28]. When a flow is imposed that produces chaotic advection it is expected that these enhancement will further increase. Tests have been done by McQuain, and Schaffer [28, 29] that show an enhancement to hybridization when the processes is conducted in a pulsed rectangular micromixing chamber intended to induce chaotically

advected flow; but there has yet to be done a comprehensive study of the flow behavior within the micromixing chamber.

In this study the nature of a chaotically advected flow within a chamber motivated by a pulsed source-sink system is examined. In particular this study characterizes the behavior of pulsed source-sink pairs activated to produce mixing in a thin rectangular chamber. The goals of this study are to numerically and experimentally characterize the mixing trends within the chamber throughout a range of pulse volumes, which are based on a percentage of the total chamber volume. This study seeks to establish a numerical model that gives useful information about the mixing in a 'real-life' pulsed source-sink system. This thesis serves as a report of the research done and discoveries revealed in pursuant of said goals. The background of Chapter I presents details of the concept of chaotic advection. It also introduces the idea of pulsed source-sink induced chaotic advection and provides a look at how the concept evolved to the present state of this study. Chapter II presents a description of the formulation of the numerical model used to simulate the pulsed source-sink mixing device, the theory behind our chaos diagnostic tools, and the results from the numerical study. Chapter III gives an account of the past experimental work done with a pulsed source-sink mixing device [29], along with the new experimental work done in this study. Comparison is made between current and previous results, and differences in the results are explained. Chapter III provides a comparison between the numerical model and the experimental results, intended to assess the validity of the numerical assumptions. Chapter IV provides a summary of the study, points out key conclusions, and remarks on future endeavors.

Background

There are two fundamental ways to describe fluid motion. The Eulerian method uses a field concept as a flow descriptor, and the Lagrangian method tracks individual particles to describe a flow [30]. The Lagrangian description of fluid motion applies to the situation of advection. When a fluid particle is advected, it follows the ambient flow, instantaneously adjusting its own velocity to that of the flow; this relation is

$$V_{particle} = V_{fluid} \tag{1}$$

Because of the kinematics of the fluid, each fluid particle in the flow is advected as such. Letting (x, y, z) be the position vector of the particle in ordinary Cartesian coordinates, the particle velocity is then given by the rate of change of its position

$$V_{particle} = \left(\frac{dx}{dt}, \frac{dy}{dt}, \frac{dz}{dt} \right) \tag{2}$$

The fluid velocity is given by methods that involve solving some set of partial differential equations, such as the Navier-Stokes equations, the Euler equations, or the Stokes equations. Representing an exact solution for the fluid velocity is not of interest, so let it be assumed that the fluid velocity components u, v, and w are solved for elsewhere and are given as a function of the Cartesian coordinates and time. This relation is shown as

$$V_{fluid} = [(u(x,y,z,t)), v(x,y,z,t), w(x,y,z,t)] \tag{3}$$

Substituting equations 2 and 3 into equation 1 gives a set of ordinary differential equations (ODEs) known as the advection equations [31],

$$\frac{dx}{dt} = u(x, y, z, t) \tag{4a}$$

$$\frac{dy}{dt} = v(x, y, z, t) \tag{4b}$$

$$\frac{dz}{dt} = w(x, y, z, t) \tag{4c}$$

According to dynamical systems theory, the ODEs of equation 4 are more than sufficient for producing nonintegrable or chaotic dynamics. The velocity components of the fluid motion do not even have to be that complicated; it has been shown that three equations with simple quadratic couplings can be nonintegrable [32].

Upon further examination of the advection equations, it can be seen that in three-dimensional flow there need not be time dependence in order to have chaos; steady flow is sufficient. When simplified to two dimensions, time-dependent flow is required to produce chaotic particle motion, because steady two-dimensional (2-D) advection is integrable [31].

In two-dimensional, incompressible flow the velocity is derived from a stream function [30],

$$u = \frac{\delta\psi}{\delta y} \quad , \quad v = \frac{-\delta\psi}{\delta x} \tag{5}$$

6

Combining equation 5 with the 2-D advection equation produces a system of equations that is in the familiar format of Hamilton's canonical equations for a one-degree-of-freedom system,

$$\frac{dx}{dt} = \frac{\delta\psi}{\delta y} \quad , \quad \frac{dy}{dt} = \frac{-\delta\psi}{\delta x} \tag{6}$$

The stream function in this case is the Hamiltonian [31]. The two-dimensional kinematics of advection by an incompressible flow is equivalent to the Hamiltonian dynamics of a one-degree-of-freedom system, and this applies regardless of whether the dynamics of the fluid itself is viscous or inviscid. There is no contradiction; incompressibility alone is sufficient to give the flow kinematics a Hamiltonian nature.

The kinematics of advection as laid out in this background, when chaotic, is commonly referred to as 'chaotic advection'. While it is believed that the general concepts behind chaotic advection have been in existence for many years [31], these ideas were not neatly formalized and the term was not officially coined until a talk given by Aref in 1982 [33].

Single Source-Sink*:*

Jones and Aref first examined chaotic advection in pulsed source-sink systems in the late 1980's [34]. The system consisted of a single source and a single sink operating in an unbounded plane and of equal strength. When the source is on, the sink is off, and when the sink is on, the source is off. A simple potential flow model was used to describe the flow from the source and sink. This study was novel because it showed the first instance

of irrotational flow displaying chaotic behavior. This result is of great interest because efficient stirring by irrotational flow would require the least amount of energy in setting up the flow field. The work of Jones and Aref was backed by both experimental and numerical results [34]. An important part of the system modeled by Jones and Aref is the way in which the fluid is extracted at the sink and then reinjected at the source. A number of different procedures can be used for reinjection. The bulk of the Jones and Aref study [34] used a 'first out – first in' method of reinjection, which can be visualized by imagining a hose connected to the sink at one end and directly to the source at the other. In this case of just one source and one sink operating in an unbounded plane trends are seen in the way the fluid interacts. Areas of periodic (non-chaotic) motion, elliptic islands, show up close to the source and sink while most of the remaining domain is chaotic (all particles initially in an elliptic island will return to the island at the end of every period). As the fluid moves away from the source and sink, towards infinity, the motion becomes more uniform and non-chaotic, with particles going off on long (far) trajectories. An example of the chaos diagnostics for this case is shown in figure 1 (Poincaré maps are created by plotting the position of a fluid particle at different times and the Lyapunov exponent is a measure of how much the particles are stretching from one another, these tools are explained in detail in Chapter II). The single unbounded plane source-sink analysis gives a good introduction into the workings of pulsed source-sink systems and serves as a foundation for future work in the field.
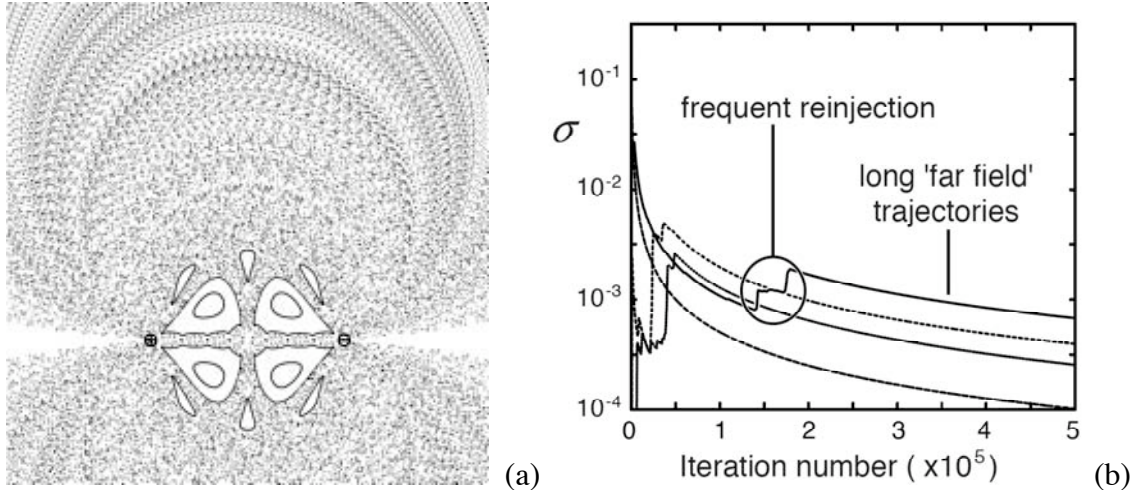
Figure 1. (a) is an example of a Poincaré map for a pulsed source-sink system on the unbounded plane. The reinjection procedure is 'first in-first out'. The source is located on the right side of the image and the sink is located on the left, denoted by a + and – respectively. The fluid area being pulsed in this case is equal to π. This result can be directly compared to figure 3(g) of Jones and Aref. (b) Convergence of the maximum Lyapunov exponent of several trajectories in the chaotic sea in (a) [3].

Source-Sink Pair:

Based on the work of Jones and Aref [34], Evans [35] proposed a MEMS device for mixing two fluids. In actual implementation of such a device a boundary is introduced that adds new parameters to the system. This boundary now requires that there be source-sink pairs in order to conserve volume in the system.

The effect of having source-sink pairs in a system is best examined on an unbounded plane before considering boundaries. The effects of adding a second source and sink to the system are illustrated in comparing the figures 1 and 2. When the distance between the paired source and sink is much larger than the distance between the non-paired source and sink, particle motion around the adjacent non-paired source and sink are the same as those found in the case of figure 1. Placing the source-sink pairs instead at the vertices of a square gives the results of figure 2. Paired sources and sinks are

9

oriented on a vertical line and operate at the same time. The dark area in the interior of the source-sink pairs is highly chaotic. The area outside this domain is similar to the trajectories in the Jones and Aref [34] case that were away from the source and sink and spent a lot of time in the far field. Particles in the 'inner-region' experience a stretching rate that is two orders of magnitude greater than the particles in the 'outer region'. Adding another source and sink, to create pairs, in general adds a higher degree of chaos to the system.

(a)　　(b)
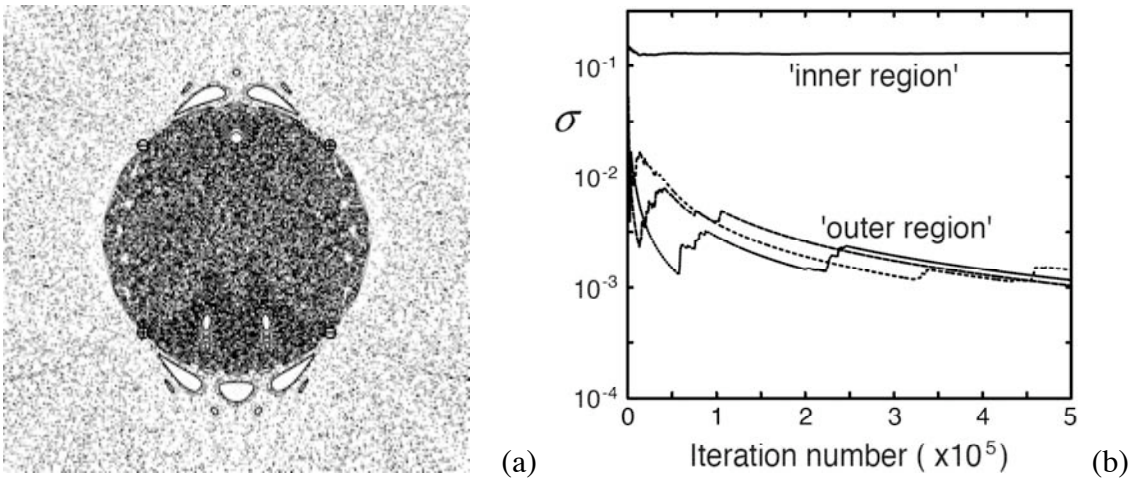
Figure 2. (a) Poincaré map for two source-sink pairs on an unbounded plane. The reinjection procedure is 'first in-first out'. The sources and sink are located at the vertices of a square with side of length 2; the paired sources and sinks are oriented on a vertical line. The sources and sink are denoted by + and – respectively. The area pulsed is equal to π. (b) Convergence of the maximum Lyapunov exponent for several trajectories in the chaotic sea of (a). The central dark chaotic sea in (a), is the 'inner region' and the chaotic sea surrounding the 'inner region' is the 'outer region' [3].

Rectangular Boundary:

Adding a boundary to a system of source-sink pairs introduces another parameter to the system. Bounding the system of figure 2 with a rectangular boundary that is of a similar

scale as the source-sink separation distance produces figure 3. Figure 3(a) uses the same reinjection procedure and source-sink configuration as used in figure 2. The analytic solution in this case assumes a slip condition at the boundary. The biggest change from adding a boundary is in the 'far-field' region. Since the fluid is no longer allowed to move far away from the sources and sink, just about all of the fluid experiences the frequent reinjection, and therefore high chaos, of the 'inner-region'. Only small areas in the corners of the domain show signs of 'far-field' effect.

Changing the reinjection procedure and source-sink configuration affects the details of the chaotic advection. In figure 3(b) the source-sink pairs lie on the diagonal as opposed to being aligned on the sides of the square, and the reinjection procedure is changed to 'last out-first in', which can be compared to collecting fluid in a tube beneath a sink, then sliding the tube to the source and reinjecting the fluid. In this configuration the corners of the domain are filled with chaotic sea, but large elliptic islands appear in the middle of the domain. Despite the details, a chaotic sea in which fluid particles are very frequently reinjected mostly dominates both of the bounded cases. Adding a rectangular boundary in addition to having source-sink pairs enhances the overall chaotic behavior of the system, allowing for a domain that is almost completely covered with a chaotic sea of frequent particle reinjection [3].
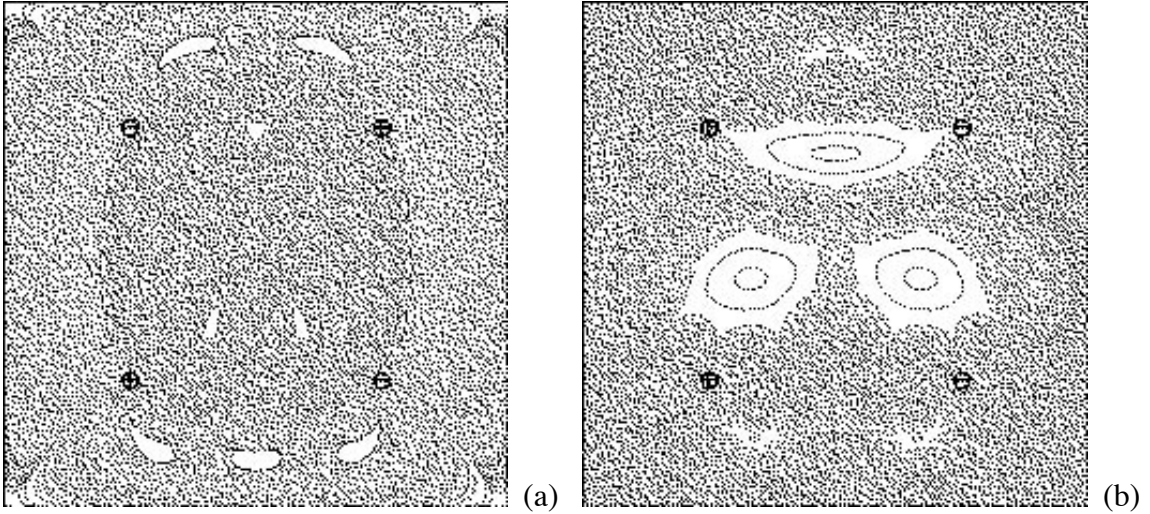
Figure 3. The Poincaré maps have sources and sinks denoted by + and – respectively. The sources and sinks are located at the vertices of a 2X2 square in a square domain with sides of length 4. The pulse area for each case is equal to π. In (a) the paired sources and sinks lie on a vertical line and the reinjection procedure is 'first out-first in'. In (b) the paired sources and sinks lie on a diagonal of the domain and the reinjection procedure is 'last out-first in' [3].

CHAPTER II

NUMERICAL MODEL

Summary

This chapter presents the results of a numerical model of pulsed source-sink mixing in a rectangular chamber. This model is used to give an analytical comparison to what happens in an actual Pulsed Source-Sink Mixing Device (PSSMD) experiment. As in the actual experiment, the only varying parameter in this numerical study is the pulse (or reinjection) volume. The pulse volume (represented as an area in our model) is varied within the range of 5 to 100 percent of the total mixing chamber volume. It is not the goal of this chapter to identify one singular pulse volume where mixing is "ideal", instead it is hoped to characterize mixing trends throughout a range of pulse volumes. In doing this it is desired to identify different ranges of pulse volumes that could be suitable for different applications.

The Model

The mixing chamber is a rectangular 3-D prism with a very small depth in relation to its width and height. For the experiments in Chapter III the mixing chamber is 71mm wide, 21 mm high, and 0.05 mm deep. By using a few fundamental assumptions, the 3-D volume of the chamber can be represented by a 2-D area. Making this reduction to a 2-D area significantly decreases computational time. A 3-D model is likely to take orders of magnitude longer to run than a 2-D model, and some of the 2-D runs can take weeks to finish

The model satisfies the no-slip boundary condition on the top and bottom of the mixing chamber. The large aspect ratio of the chamber means that the boundary conditions on the top and bottom of the chamber dominate the behavior of the flow. This allows one to relax the boundary conditions on the sides of the mixing chamber and model the sides as forced streamlines of the flow; that is, no flow is allowed through the outer walls but slip is allowed along them. The flow can be viewed as a Hele-Shaw flow (flow with Re << 1 between two parallel plates), which is governed by the Stokes flow approximation. Under these approximations, a velocity potential can represent the depth-averaged velocity. Thus, assuming that the depth-averaged velocity determines the transport of molecules across the surface, the chamber can effectively be modeled using two-dimensional potential flow. The flow in this case will transport molecules on a time scale much shorter than that of diffusion, so it is expected that the flow kinematics will provide a good representation of the overall molecule dynamics.

In deriving the model each source and sink is given the same strength, q, which is equal to the product of the pulse volume (area in the model) and the amount of time a given source or sink is on. Superposition of a source located at $Z_p = X_p + iY_p$ in the complex plane and a sink at Z_n produces the complex potential [36],

$$F(z) = \frac{q}{2 \cdot \pi} \cdot \left(\log\left(z - z_p\right) - \log\left(z - z_n\right) \right) \tag{7}$$

which is for flow in an unbounded domain. The equation can be modified for a variety of bounded domains by conformal mapping of the z-plane to the w-plane. The rectangular

domain can be obtained by conformal mapping of the upper half plane onto a rectangle using a Schwarz-Christoffel transformation. Using the method of images the upper half plane complex potential is found to be [36]:

$$F(z) = \frac{q}{2\pi}\left[\left(\log(z - z_p)\right) + \log\left(z - \overline{z_p}\right) - \log(z - z_n) - \log\left(z - \overline{z_n}\right)\right] \qquad (8)$$

This plane is mapped to the interior of a rectangle by using the transformation

$$w = f(z) = \frac{1}{2}\left(1 + sn(K(k)\,z, k)^{-1}\right) \qquad (9)$$

where the Jacobian elliptic sine is sn(z,k), and K(k) is the complete elliptic integral of the first kind. The parameter k is determined by the aspect ratio α of the domain [36]

$$\alpha = \frac{K\left(\sqrt{1 - k^2}\right)}{2\,K(k)} \qquad (10)$$

The geometry of the model is a 71 mm x 21 mm rectangle. The sources and sinks in the model are placed at a 2.5 mm offset (measured to the center of the source or sink) from the corners of the rectangle. The sources and sinks are located relative to each other as shown in figure 4.

15
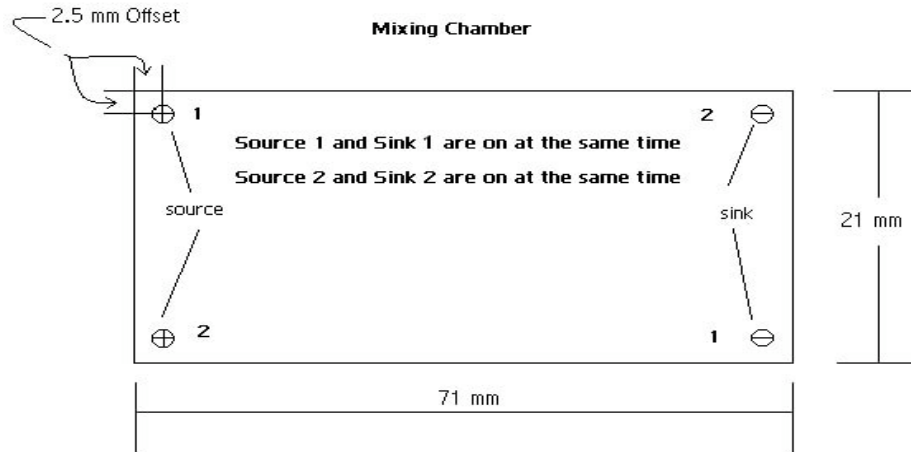
Figure 4. Geometry, dimensions, and source-sink location used in the numerical model.

The model uses a 'last in-first out' reinjection procedure that can be realized by picturing fluid being extracted with a syringe at the sink and then being forced back out the way it came in at the source. It is thought that the 'last in-first out' protocol is a good representation of what is currently being done in experiments. With the 'last in-first out' protocol there are two options on how to treat the behavior of a fluid particle as it enters through a sink and leaves through a source. First, one can allow the particle to remember its entrance angle upon exit, as a result exiting at an angle rotated 180 degrees from its entrance angle. This case will be referred to as the 'remembered angle' case. This case is the most conservative in regards to evaluating mixing; it allows for the formation of elliptic islands, which will be explained later. For the other case, one can allow the particle to reenter the chamber at a random angle. This case will be referred to as the 'random angle' case. This case is much less conservative in regards to evaluating mixing; it does not allow for the formation of elliptic islands. These different reinjection

16

angle methods will be used to develop a deeper understanding of the chaos trends with changing pulse area.

For this model the parameter that is varied in search of "optimal chaos" is the pulse area. Pulse area is a function of pulse time and pulse strength (pulse area = pulse time * pulse strength). This pulsing of the fluid is key to the development of chaotic advection in the flow and the expected possibilities of optimal mixing.

Numerical Analysis Tools:

Four different tools are used to examine the results of the analytical chaotic advection model: Poincaré maps, Lyapunov exponents, a particle density model, and a variance analysis. It is desired to determine the system parameters for which (1) the domain is dominated by the chaotic sea (as indicated by the Poincaré map and particle density analysis) and (2) the fluid within that chaotic sea is stretched most rapidly and distributed most evenly (as indicated by the Lyapunov exponents, particle density analysis, and variance analysis).

Poincaré maps and Lyapunov exponents are computed by numerically integrating a given particle forward in time under the constraint that during a cycle of operation the particle remains on its streamline, which is constant. The Poincaré maps are created by following a fluid particle's trajectory through several periods (or pulses) of operation and recording the position of the particle after every period. For each period, the particle travels along a constant streamline, which is a function of the velocity potential that governs the flow associated with the source and sink on during that particular period. Figure 5 is an illustration of the streamlines associated with each source-sink pair.
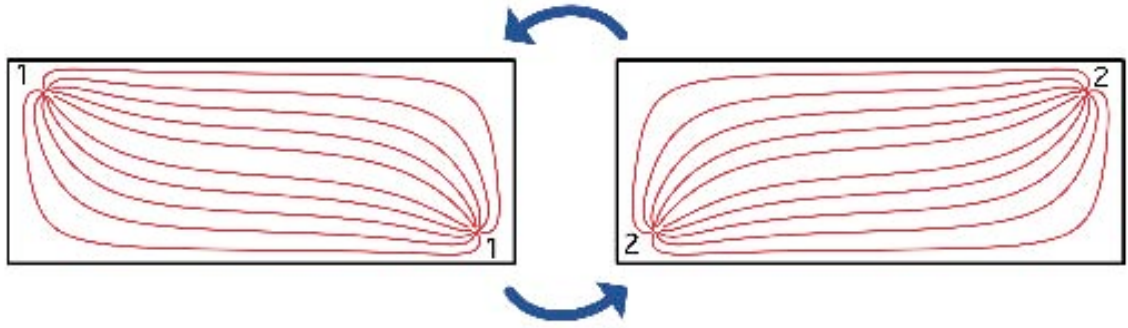
Panel (a)   Panel (b)

Figure 5. Panel (a) shows when source 1 and sink 1 are on, and panel (b) shows when source 2 and sink 2 are on.

At the end of each period the particle's position is recorded, and then used as a starting position for the next period. As a result of having source-sink pairs, there are two different velocity potentials (a potential for each source-sink pair on, while the other pair is off), and therefore two sets of constant streamlines that govern the flow behavior. The particle switching back and forth between streamlines is what creates the 'stretching' effect on the flow field. Figure 6 is an illustration of a fluid particle's path over several periods, with the particle trajectory switching back and forth between streamlines as mentioned before.
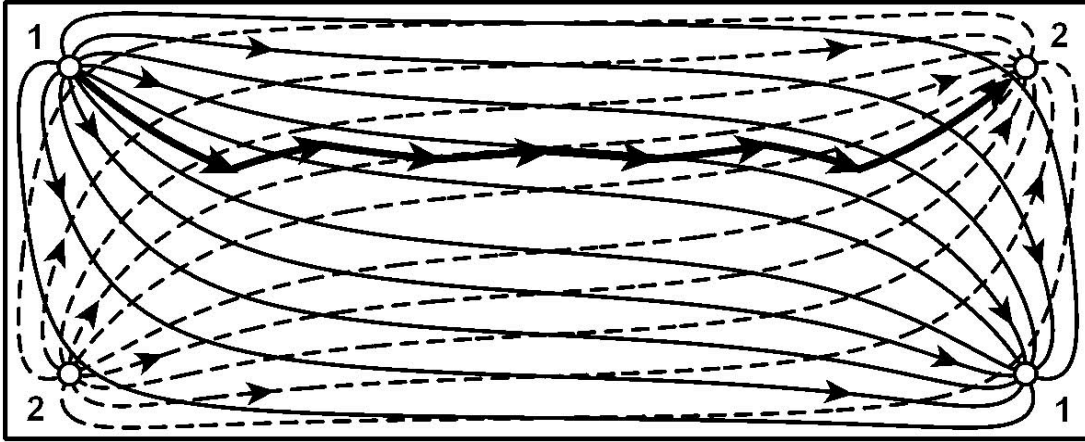
Figure 6. Advection of a particle due to pulsed source-sink operation.

The Poincaré maps consist of two main parts: The chaotic sea and elliptic islands. In the chaotic sea, particle trajectories are not periodic; a particle will never return to the same location twice, and then as time goes to infinity that particle will visit every available position within the chaotic sea. Fluid within the chaotic sea experiences exponential stretching, which is expected to produce enhanced mixing. The more a fluid is stretched (and folded) the better it is mixed. In general mixing occurs naturally when two miscible fluids have a concentration gradient between them. In a chaotic sea the interface between these fluids is stretched exponentially, which rapidly increases the interfacial area across which diffusion occurs. A good analogy to the relation between stretching and mixing is the process of kneading dough. The dough is stretched out then folded over, and the process is continually repeated until the dough is mixed. The elliptic islands are areas in which particle trajectories are periodic, and a particle will be trapped within this region, meaning that all particles initially in an elliptic island will return to that same elliptic island at the end of each period. The elliptic islands are characterized by only linear stretching, which is expected to produce poor mixing. These periodic

19

particle trajectories, elliptic islands, are dependent on the particle having some ability to remember the angle at which it enters the sinks upon exit from the sources. On a Poincaré map the chaotic sea shows up as dense, somewhat uniform, areas of color, whereas the elliptic islands show up as "holes" in the map. An indication of an ideal mixing situation would consist of maximizing the chaotic sea and minimizing the amount and/or size of elliptic islands on a Poincaré map. Poincaré maps show how much of the domain experiences exponential stretching (or how many of the initial particles will be in a chaotic region). Another diagnostic tool, the Lyapunov exponent, gives the size of the exponent for the exponential stretching. The Lyapunov exponent is calculated for both stretching over time and stretching over period. The Lyapunov exponent is calculated by following two particles throughout time or over a period and measuring how fast they move away from each other. Imagine there is a line of length, L, connecting two fluid particles. As time (once again this can be period, we would just need to substitute p for t), t, approaches infinity, the Lyapunov exponent, σ, is given by:

$$L = L_0 \cdot e^{\sigma t} \qquad L_0 = \text{initial Length between particles} \qquad (11)$$

$$\sigma = \frac{\ln\left(\dfrac{L}{L_0}\right)}{t} \qquad\qquad \sigma = \lim_{t \to \infty} \lim_{L \to 0} \frac{\ln\left(\dfrac{L}{L_0}\right)}{t} \qquad (12)$$

The strongest chaos over time or period occurs when the Lyapunov exponent is largest; in contrast, within the elliptic islands the Lyapunov exponent is zero.

The third diagnostic tool is a particle density map. The map is used to approximate how much of the domain is covered by the chaotic sea. Dividing the mixing chamber

domain into bins creates the map; this is done numerically in the form of a matrix. The

mixing chamber is divided into 4940 bins for this analysis. This bin number was chosen

by normalizing the data so that the pulse area that gives the greatest coverage is the only

one that gives zero empty bins. Each case is then run for 50,000 periods, producing

approximately 100,000 data points (this is because in the model two points are tracked at

the same time). The amount of points in each bin is tallied and the number of empty bins

is recorded for each case. The result is used to determine the percentage of the domain

covered by the chaotic sea. For the random angle case the particle density map is used to

show how randomly distributed the particles are across the domain. This is done by

applying color intensities, to the bins of the matrix, scaled by the number of points in a

particular bin; the matrix is then plotted.

The finial diagnostic tool is a variance analysis. The variance analysis is used to

better illustrate how randomly distributed the points are across the domain. The variance,

c-bar, is calculated as

$$c_{bar} = \sum_{i=1}^{N} \frac{\left(1 - \frac{c_i}{c_{max}}\right)^2}{N} \tag{13}$$

c_{bar} = variance

c_i = number_of_points_in_a_given_bin

c_{max} = max_number_of_points_in_any_one_bin

N = total_number_of_bins

Results

The system parameters that effect the time it takes to get enhanced chaos is considered, and insight is provided into the balance between time and enhanced chaos as it may apply to different applications.

In an attempt to understand the effect of pulse volume on the chaos characteristics in the mixing chamber several test are run ranging from a pulse volume of 5% to a pulse volume of 100% of the chambers total volume. Test are run in increments of 5% and note is made of trends observed in the Poincaré maps. These tests are run using the remembered angle case. The number and size of elliptic islands present on a given Poincaré map is used as a first indication of the presence of optimal chaos. It is observed that the pulse volumes of 5%, 10%, 15%, 20%, 25%, 30%, and 35% produced multiple small elliptic islands that gradually shift to a few large elliptic islands as the pulse volume increases. The elliptic islands in each case are distributed throughout the domain in a somewhat set, consistent pattern. This pattern and the changes in elliptic island size are shown in figures 7-10.
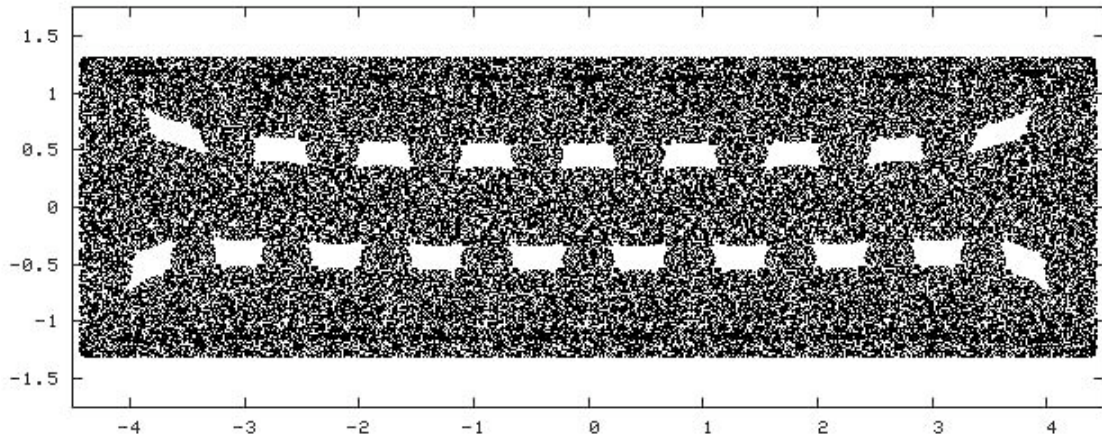
Figure 7. Pulse Volume is equal to 5%. It should be noted that in this case a particle has a tendency to stay on one side of the domain for a long time.
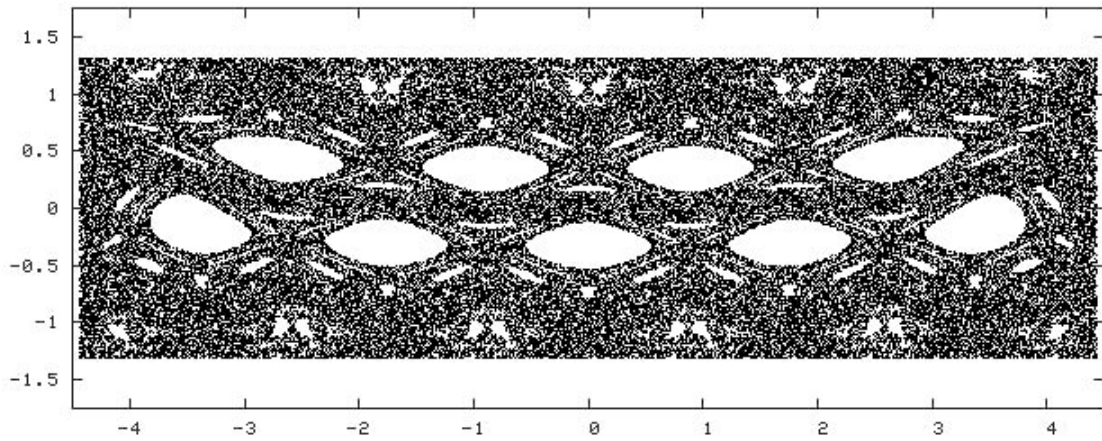
Figure 8. Pulse volume is equal to 10%.
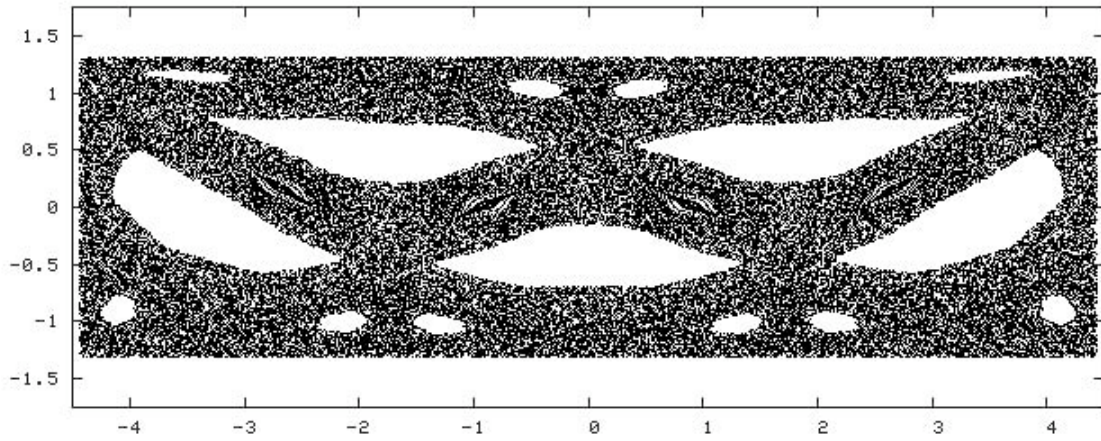
Figure 9. Pulse volume is equal to 20%.
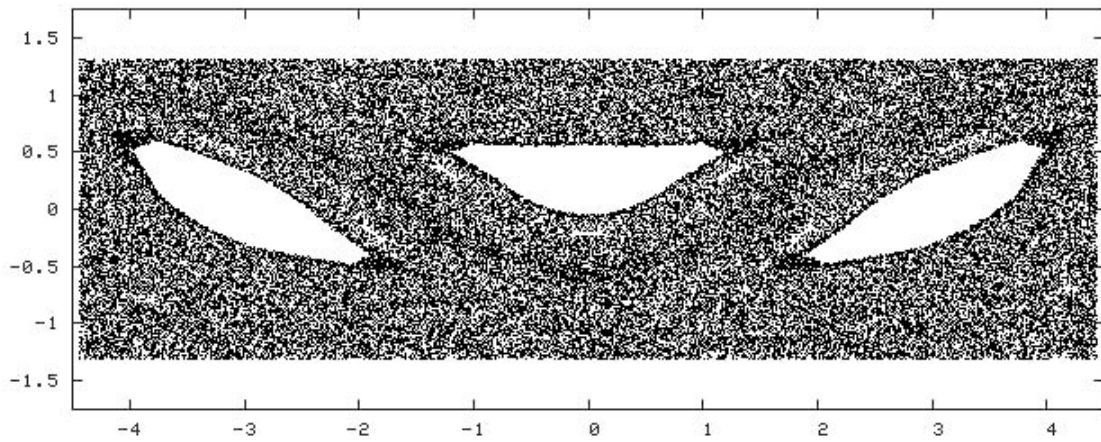
Figure 10. Pulse volume is equal to 35%.

It is observed that the pulse volumes of 40% and 45% produced just a few small elliptic

islands. Figure 11 is an example of a Poincaré map for this case.
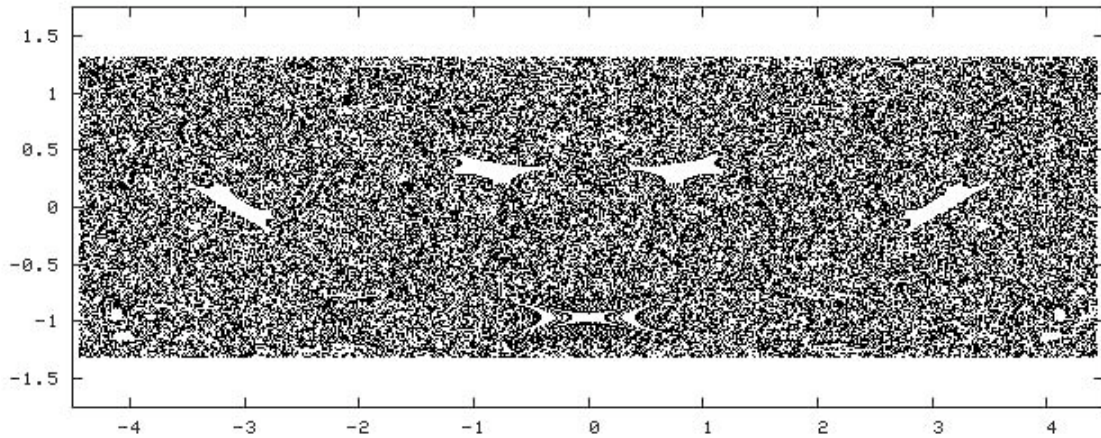
Figure 11. Pulse volume is equal to 45%(in the 40% case the domain is almost completely covered by the chaotic sea).

It is observed that the pulse volumes from 50% to 100% produced a trend of increasing

elliptic island size with increasing pulse volume. One large elliptic island begins to show

up in the middle of the domain at a pulse volume of 60%, and it grows larger with

increased pulse volume. Thus, the Poincaré map pattern is the same for pulse volumes of

70% to 100%. The Poincaré maps in figures 12-14 show the discussed trend.
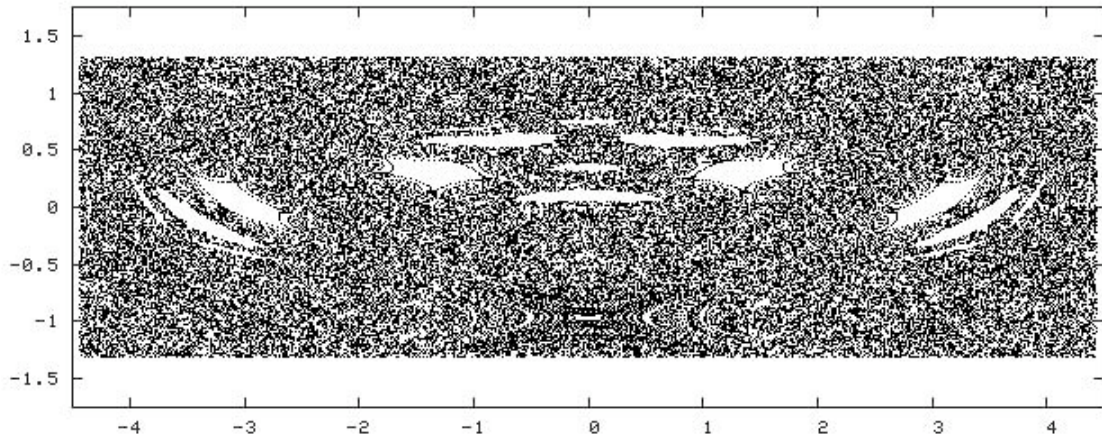
Figure 12. Pulse volume is equal to 50%.
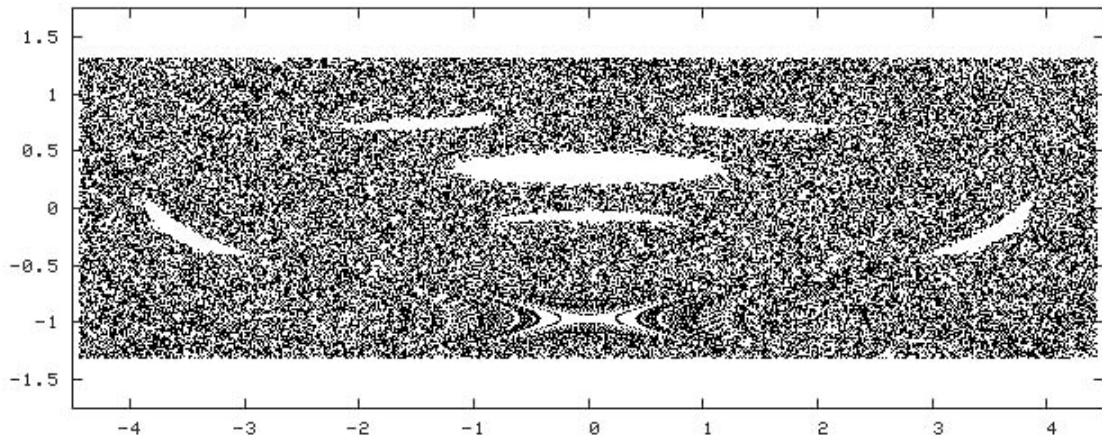
Figure 13. Pulse volume is equal to 60%.
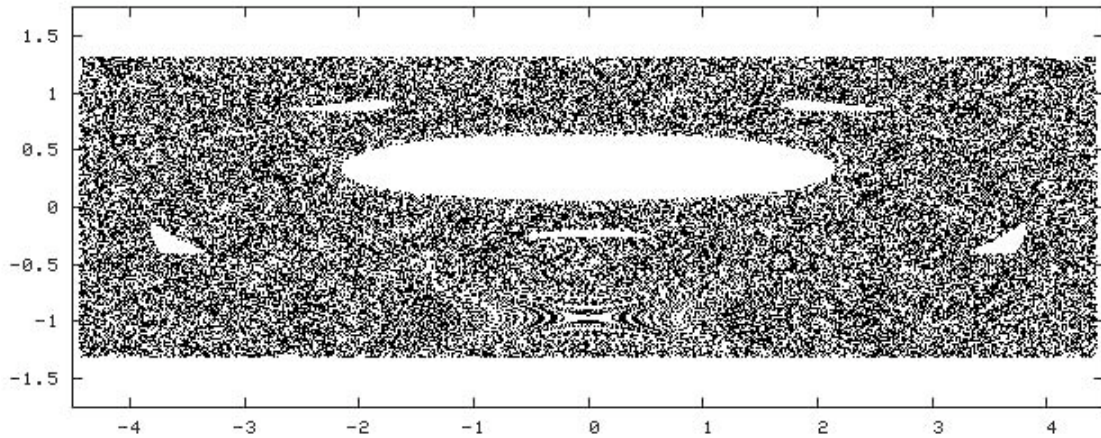
Figure 14. Pulse volume is equal to 70%(from 70% to 100% the only change is the size of the center elliptic island; it gets bigger).

The Poincaré maps show the amount of the domain covered by the chaotic sea. From examining the Poincaré maps one is able to identify ranges of pulse volume that indicate a possibility of optimal mixing. In order to quantify the coverage it is necessary to do a particle density analysis. The density analysis is done to determine an approximate percentage of the domain that is covered by the chaotic sea. The results of this analysis are shown in figure 15.

Chaotic Sea Coverage of Total Domain
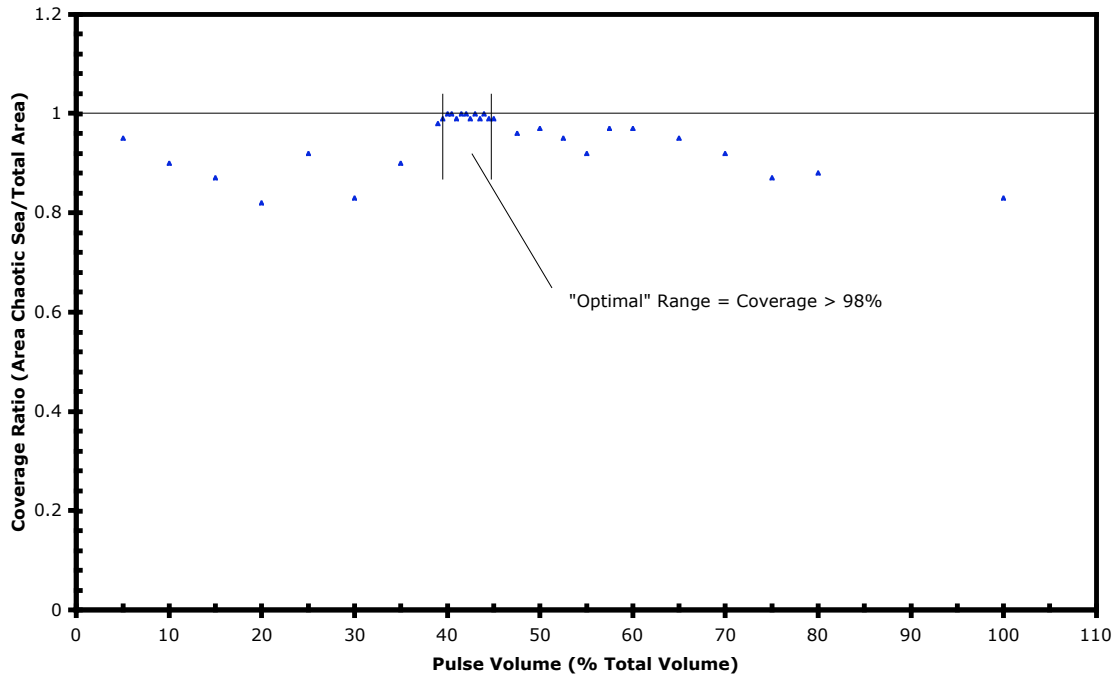
Figure 15. Plot of the amount of the mixing chamber domain that is covered by the chaotic sea as a function of pulse volume.

It must be noted again that in the 5% pulse volume case a particle has a tendency to stay in one side of the domain for a long time. The results show the 5% case as having about 95% coverage of the domain, but it is best to view this as two half domains with 95% coverage. It can be seen from Figure 15 that the pulse volumes in the middle range, as classified in our Poincaré analysis, provide a high chaos coverage ratio for the domain space. For pulse volumes larger than this range the domain coverage decreases, sloping downward to a low at 100%. For smaller pulse volumes the trend is a little more complex, but it appears as if the best chaotic sea coverage in this range occurs in the smallest pulse volumes (5%, 10%, 15%).

Knowing how much of the domain is covered by the chaotic sea is an important process, but it only tells part of the story in regards to understanding how well the mixing might be in the domain. The Lyapunov exponent, as explained before, is a measure of the magnitude of the exponential stretching in the chaotic sea. By looking at the Lyapunov exponent one can get an idea about the level of potential mixing within the identified chaotic sea. The higher the Lyapunov exponent the faster fluid particles are stretched over time (period). In the analysis of Lyapunov exponents, the convergence of the Lyapunov exponent over time (period) for each pulse volume ran, is examined. This number is multiplied by its respective chaotic sea coverage ratio, for each pulse volume. This new value is a measure known as the Kolmogorov entropy, which gives a comparison of the 'total chaos' in the entire mixing domain. The results of this analysis are shown in figure 16.

Comparison of Exponential Stretching Over Time to Exponential Stretching Over Period
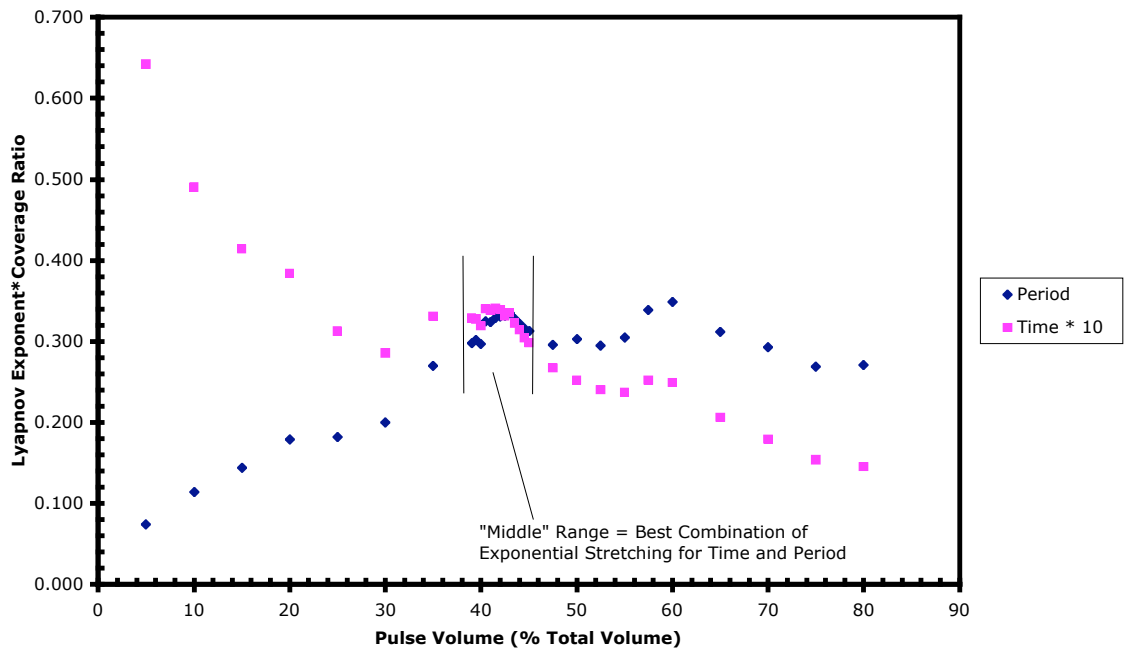
Figure 16. The numeric value of the Lyapunov exponent for stretching over time is an order of magnitude less than the Lyapunov exponent for stretching over period, so for better graphical comparison the time exponent is scaled up. This scaling is allowed because we are interested in trends, and not so much numerical values.

As seen in figure16 the Lyapunov exponent for stretching over time generally decreases with increasing pulse volume. There are small ranges where the behavior is different. The behavior for the Lyapunov exponent for stretching over period is to generally increase with increasing pulse volume; again with small areas behaving differently. As a note it has been observed for pulsed source-sink mixing on an unbounded domain that the trends of the Lyapunov exponent behavior over pulse volume are similar to this bounded case, the only difference is that in this bounded case there are small ranges of pulse volume that display unique behavior. This unique behavior is thought to be the result of having bounded geometry, in general, but in this particular case the rectangular geometry

30

of the mixing chamber. To better understand the unique behaviors of this case one can look at ranges of the chart in figure 16. The lower range (5%-35%) Lyapunov exponents present some interesting results. The stretching over time in particular is found to be very high in the small pulse volumes, with the time Lyapunov exponent for 5% being almost double the average for the rest of the pulse volumes. Equally, the stretching over period in the lower range is very low. What happens in the lower range is not unexpected. The stretching over the period is expected to be small for small pulse volumes (which correspond to short periods), because there is not enough time in the period for any significant stretching to occur. On the other hand, the stretching over time is expected to be large, because of the rapid fluid stirring created by the frequent switching of source-sink pairs associated with short periods (or pulses). The middle range (39%-45%) Lyapunov exponents show an interesting trend of 'humping' up to higher values for both time and period stretching. This middle range offers the best combination of stretching over time and period. This characteristic of having the best combination of stretching over time and period is not unexpected. The interesting surprise in this case is the 'humped' or higher values experienced in this range. The upper range (47.5%-80%) shows some unique behaviors that go against the general trend of the data. From 47.5% to 60% pulse volume the Lyapunov exponents over period and time start to level off a bit, then each case begins to show a trend that is similar to the other. From 60% pulse volume on to 80% both the Lyapunov exponent for stretching over time and period start to slightly decrease. In the case of stretching over time the decreasing Lyapunov exponents is expected, because the longer periods allow for more constant streamline motion over time. The decreasing Lyapunov exponents for stretching over period in this

case are less expected. This is thought to be caused by a combination of the present geometry and the large amount of the volume being pulsed. For high pulse volumes there is a tendency for fluid to stay in the injection tubes for a larger percent of the period, thus causing that fluid to be stretched less over the period.

For practical applications of pulsed source-sink mixing in a rectangular chamber, the Lyapunov exponent for stretching over time will give the best idea of the potential mixing in the chamber. Two important variables to consider in looking at practical applications are the time it takes to get a level of mixing, and the level of mixing achieved in that time. The ideal situation would be fast and 'good' mixing. To this point, the coverage of the chaotic sea and how well particles are stretched within this sea are examined as a way of classifying fast and potentially 'good' mixing. In order to further one's understanding of this system, this study will now look at how randomly the fluid particles are distributed across the domain; to do this the model is run using the random angle reinjection case. In reality the reinjection angle will be somewhere in between the remembered case and random case, remembered being the lower bound on the prediction of enhanced mixing and random being close to an upper bound. By reinjecting the particles at a random angle it destroys any periodic sections of the domain, thus not allowing for the development of elliptic islands. Using the variance and particle density diagnostic tools it is desired to determine how evenly fluid particles are distributed across the mixing chamber domain and how fast a decently even distribution is achieved.

The variance of the particle distribution over time is calculated for this analysis. This calculation is done by dividing the domain into bins and counting the number of particles

in each bin at different time steps. 5000 bins is initially chosen as the bin number, but the

analysis is run at 10000 and 1000 bins to see how the number of bins affects the trend of

the data. Figures 17-19 show the variance over time for pulse volumes in the lower,

middle, and upper ranges. The volumes are 5%, 10%, 41.5%, and 100%.
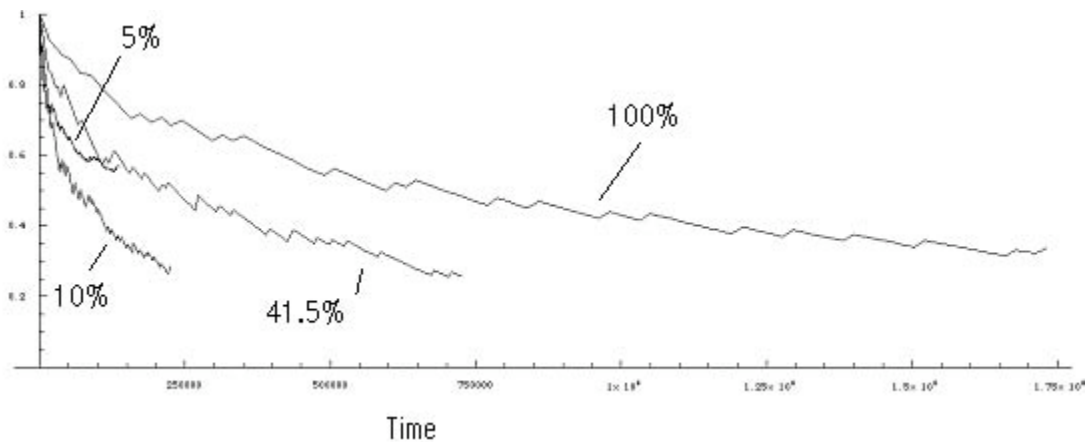
Figure 17. For this chart the domain space is divided into about 5000 bins, and then the
variance of particles distributed across the bins is calculated as a function of time.
Displayed on this chart are pulse volumes of 5%, 10%, 41.5%, and 100%.
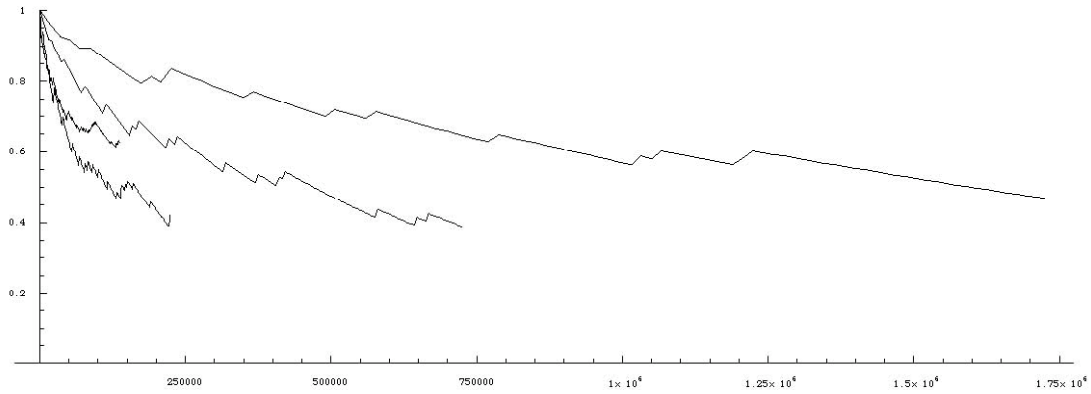
Figure 18. For this chart the domain space is divided into about 10000 bins, and then the variance of particles distributed across the bins is calculated as a function of time. Displayed on this chart are pulse volumes of 5%, 10%, 41.5%, and 100%.
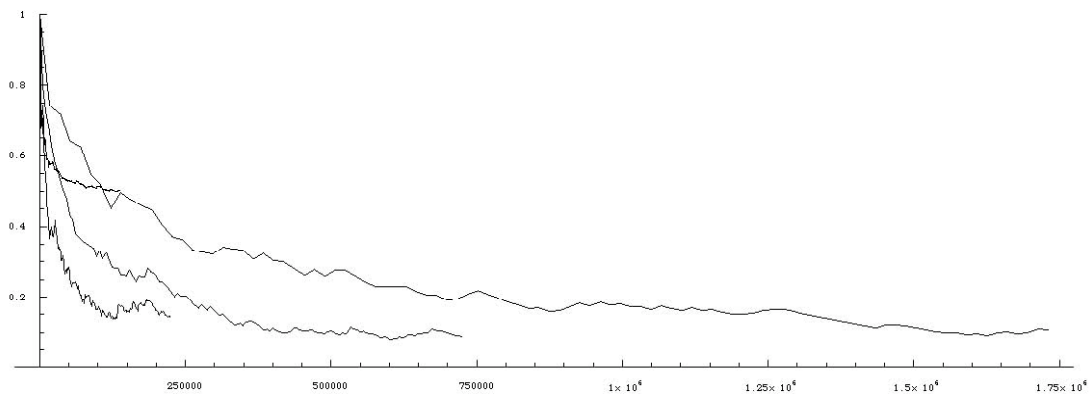
Figure 19. For this chart the domain space is divided into about 1000 bins, and then the variance of particles distributed across the bins is calculated as a function of time. Displayed on this chart are pulse volumes of 5%, 10%, 41.5%, and 100%.

The data shows a consistent and similar trend for each bin number chosen. This leads one to believe that the number of bins used has little effect on the variance trend, so for the rest of the analysis a bin number of 5000 is used. From figures 17, 18, and 19 it can be seen that two of the cases, pulse volumes 10% and 41.5%, show good signs of even particle distribution and getting to that even particle distribution fast. The 41.5% case gets to the most evenly distributed state, but it takes a little longer to get there. The 5%

and 100% case show signs of leveling off at a high variance and taking a very long time to reach a low variance respectively. The variance of the 5% case is greatly effected by the tendency of a particle to get trapped on one side of the domain, as shown in particle density image of figure 20.
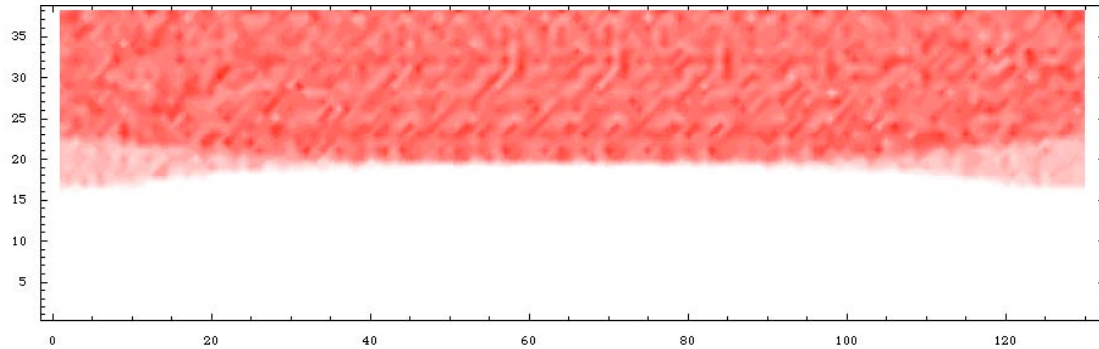
Figure 20. Particle density image for 5% pulse volume.

In the middle range the lowest variances are achieved. From 40% to 45% the variance of the particle distributions approach a value around 0.275 as seen in the figure below.
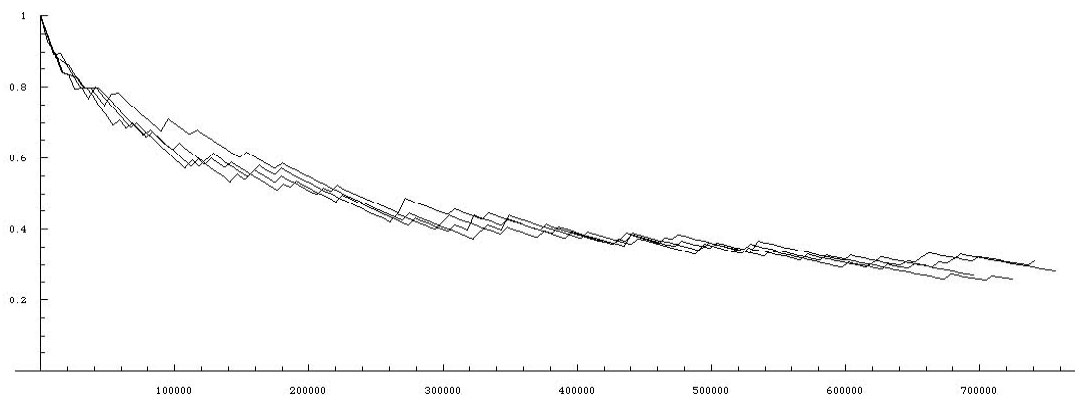
Figure 21. Variance analysis for pulse volumes of 40% to 45% (Middle range).

In the lower range, the pulse volumes of 10% to 20% approach variances that reach about 93% of the value of the middle range (around .295), but they approach these values in 32% to 57% of the time it takes the middle range to approach its values. Figure 22 shows the variances of the lower range.
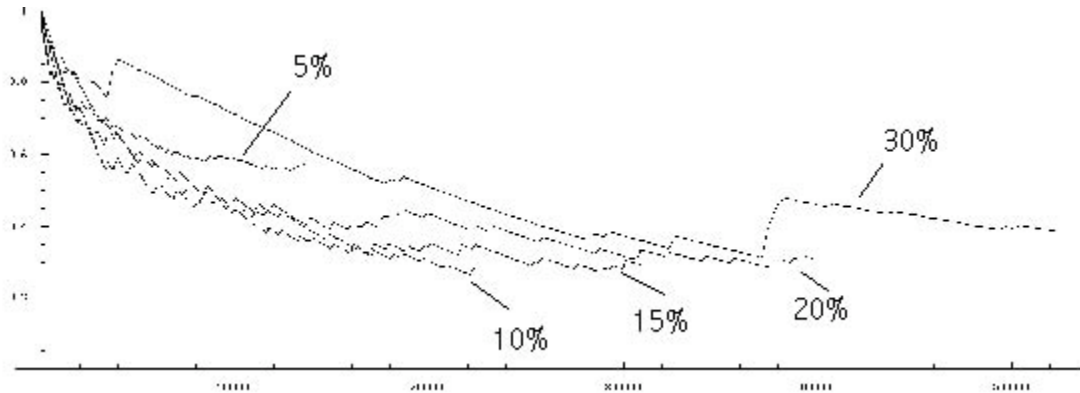
Figure 22. Variance analysis for pulse volumes of 5% to 30% (lower range).

The particle density images of figures 23 and 24 show the slight difference in the distribution of particles for the lower range compared to the middle range.
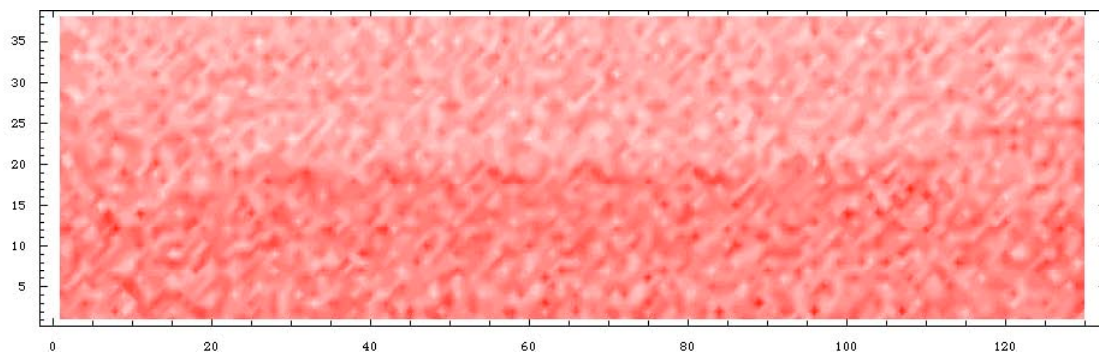
Figure 23. Particle density image for 10% pulse volume (in lower range).
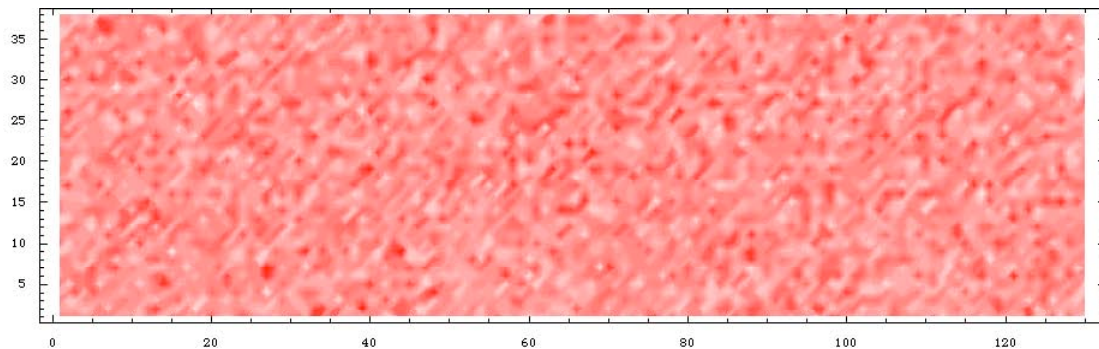
Figure 24. Particle density image for 41.5% pulse volume (in middle range).

The variances in the upper range go from 0.29 up to 0.34 with increasing pulse volume as seen in figure 25.
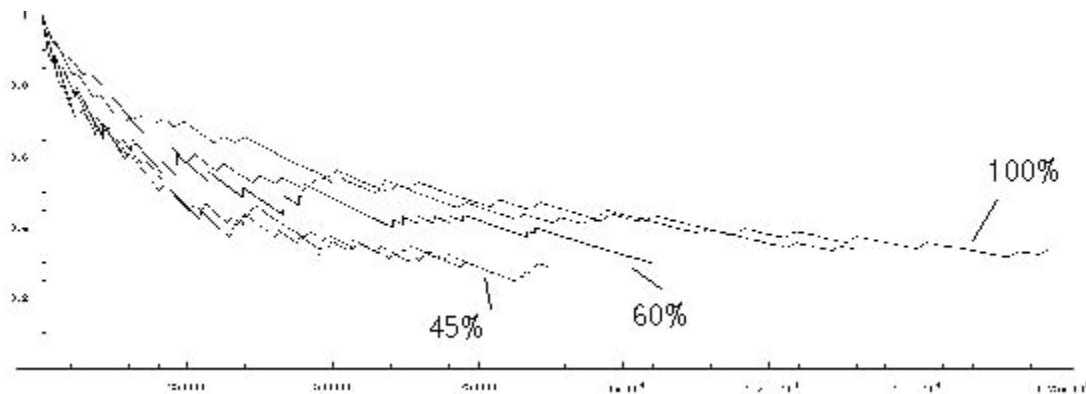
Figure 25. Variance analysis for pulse volumes of 45% to 100% (upper range).

In the upper range it takes increasingly longer times to reach increasingly higher variances with increasing pulse volume. The trends displayed in the upper range point towards less optimal mixing in that range.

37

Conclusion

In this numerical model of a rectangular pulsed source-sink mixing chamber, it is desired to understand how the parameter of pulse volume affects certain indicators of potential good or bad mixing. Those indicators are the amount of coverage of the chaotic sea, the exponential stretching within the chaotic sea, and how evenly particles are distributed over the chamber volume. The results of this study show that there is more that one range of pulse volumes that can be applied to produce positive indicators of optimal mixing. In the lower range, pulse volumes of 10% to 20% produce positive indicators of optimal mixing. For the conservative remembered angle method these pulse volumes cover 82% to 90% of the domain with chaotic sea. The chaotic sea coverage is a little low in comparison to the best coverage displayed, but it has relatively high exponential stretching. For this range of pulse volumes the particles are evenly distributed across the domain 32% to 57% faster than the middle range, which is the next best case. This range approaches a variance of about 0.295, which is about 93% of the best variance achieved, 0.275. The pulse volumes of 10% to 20% can be classified as providing potentially fast and close to optimal mixing. The middle range, with pulse volumes of 40% to 45%, produces positive indicators of optimal mixing. For the remembered angle method the middle range pulse volumes cover 98% to 100% of the domain with chaotic sea. The exponential stretching within the chaotic sea is high, although not quite as high as in the case of pulse volumes of 10% to 20%. For the middle range pulse volumes it takes a little longer for the particles to be evenly distributed across the domain, but in the end this range reaches the best variance, 0.275. The middle range pulse volumes can be classified as providing potentially 'fast enough' and optimal mixing. The upper range, 45% to

100%, can best be classified as providing the least optimal mixing, by all indications. In the upper range the potential mixing gets less favorable with increasing pulse volume. An interesting case that shows potential for enhanced mixing is a pulse volume of 5%. In this case a particle has a tendency to stay on one side of the domain, but on that side the coverage of the chaotic sea is high, 95%, and the exponential stretching is almost double that of other cases. In the 5% case the particles are evenly distributed across the half domain faster than in any other case. This case can best be described as providing potentially fast and optimal mixing to limited applications.

CHAPTER III

PHYSICAL MODEL

Summary

This chapter presents the results of experiments involving a pulsed source-sink mixing system with a rectangular chamber. These results will be compared with the numerical results presented in Chapter II, so as to provide a rigorous analysis of the mixing system behavior. The work presented here will build on and expand upon previous work [29]. A review of previous work with a Pulse Source-Sink Micromixing Device [29] is presented in the beginning of this section. This chapter will characterize experimental trends within the mixing chamber, through a range of pulse volumes.

Previous Experimental Work

The focus of previous work [29] is to improve upon the process of microarray hybridization. To do this a Pulsed Source-Sink Micromixing device (PSSMD) is designed. This PSSMD is also used in this study, although the assembly procedure and components are modified. The previous work seeks to improve the hybridization process by incorporating the principles of chaotic advection into the mixing device design and secondly reducing the amount of analyte and solution necessary by the nature of the PSSMD's microfluidic components.

An important aspect of the previous work [29] is the inclusion of the PSSMD plumbing on the device itself. This on-device microplumbing is created by the use of PDMS, an advanced polymer substance [29].

The PSSMD operating cycle is designed with the inspiration of previous work that studied a planar, laminar mixer [29, 35]. The cycle is setup so that there are four ports connecting the mixing chamber to four external channels. Channels that operate on alternating cycles are linearly aligned on one side and connected at a junction that leads to one of two independent reservoirs. Each of the four channels has a check valve that restricts the flow to one direction. Figure 26 shows a description of the PSSMD cycle. On the half-cycle valves 2 and 4 are closed. Fluid from reservoir A is injected and flows into the chamber at port 1 (source). Fluid flows out of the chamber at port 3 (sink) and is collected in reservoir B. On the full-cycle valves 1 and 3 are closed. Fluid form reservoir B is injected and flows into the chamber at port 2 (source). Fluid flows out of the chamber at port 4 (sink) and is collected in reservoir A. This operating cycle is designed to produce chaotic advection in the chamber and a fluid particle motion as illustrated in figure 6. Schaffer's experimental setup consists of four modules: The PSSMD, Pumping Unit, Control Unit, and Valving Unit. A schematic of this setup is show in figure 27.
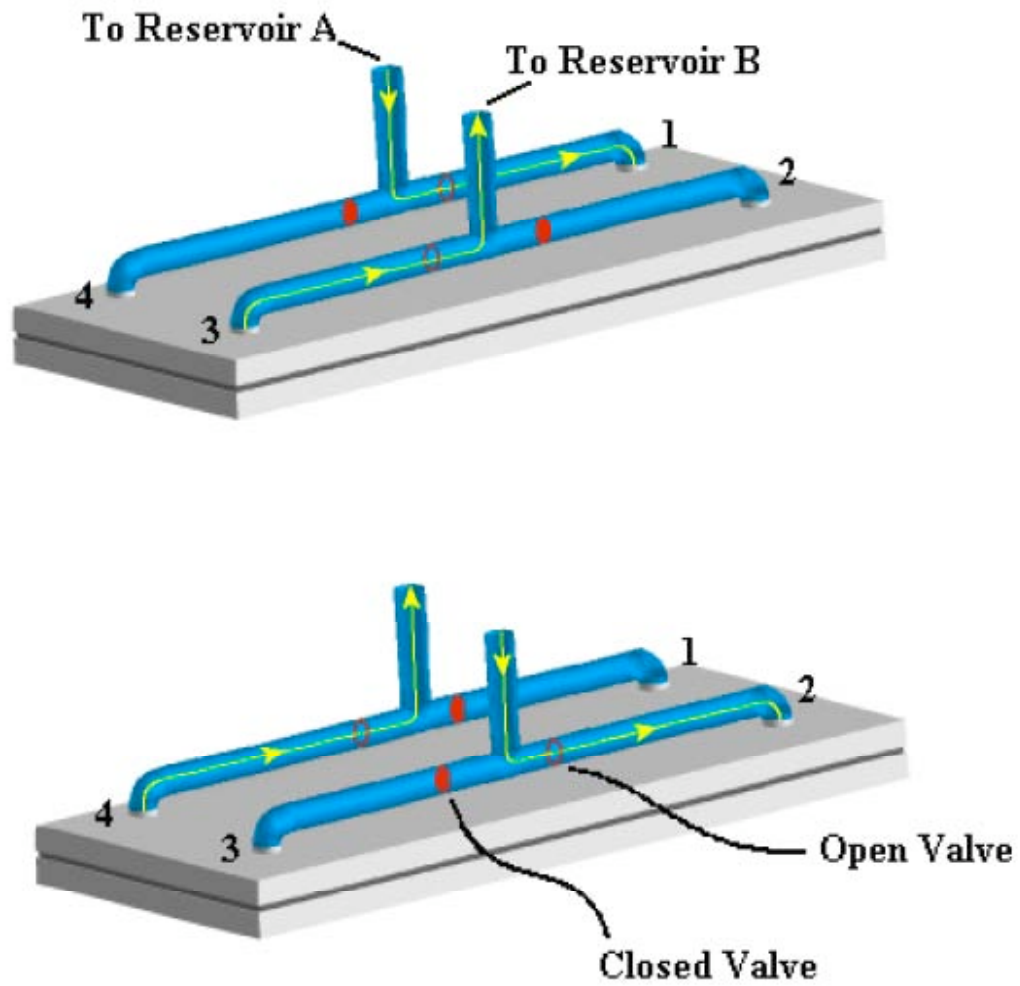
Figure 26. Conceptual view of the PSSMD cycle. In this configuration, port 2 is the source and port 4 is the sink [29].
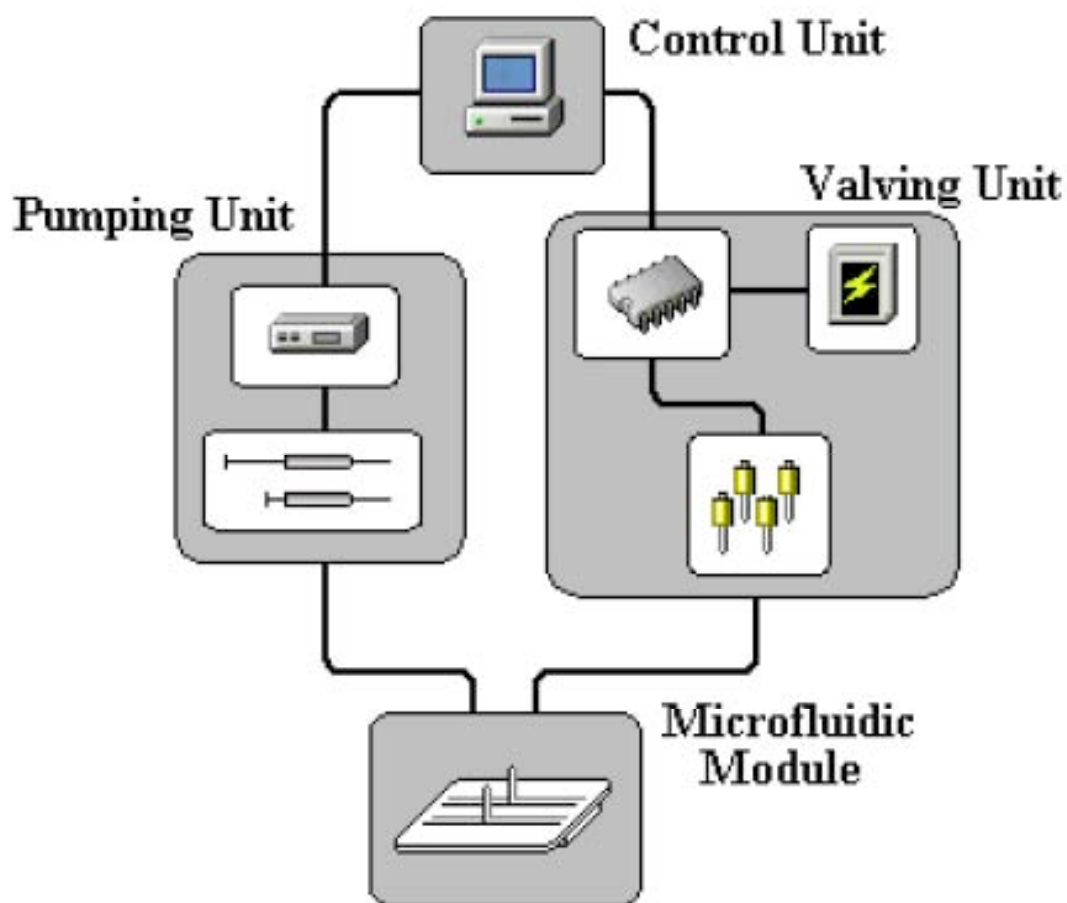
Figure 27. Schematic of PSSMD . The Control Unit, which is a PC, commands the Valving Unit and the Pumping Unit using a custom LabVEIW Virtual Instrument. The Valving Unit is comprised of a relay circuit, a DC power supply, and an array of four solenoid actuators. The pumping Unit consists of a slave controller and two syringes, each mounted in a motorized syringe pump. The Microfluidic Module is the mixing chamber and the on-board microchannels [29].

The control unit governs the behavior of the valves and pumps. The unit is a custom LabVIEW (National Instruments Corporation, Austin, TX) Virtual Instrument application run on a desktop PC. The VI is interfaced with the valves by a digital I/O card connected to the PC. The VI controls the pumping unit through a serial port on the PC where the pumps slave controller is connected. The VI control unit allows the user to control

experimental parameters such as injection volume, flow rate, flow direction, valve activation/ relaxation time, and number of pulse cycles. The pumping unit is made up of two independently controlled syringe pumps (World Precision Instruments, Inc., Sarasota, FL). Each pump is equipped with a 500 μl syringe (Hamilton Company, Reno, NV). Vinyl tubing is used to connect each syringe to a steel port on the top of the Microfluidic Module. The pumps are wired to a slave controller that is connected to the control unit. The pumps are configured so that they can be controlled manually or automatically. The valving unit consists of four solenoid actuators (Bicron Electronics Company, Canaan, CT). When energized these solenoids will pinch closed the on-device microchannel beneath it. Upon relaxation the channels reopen due to the resilience of the PDMS material. This pinch valve system proves to be very efficient [29]. The I/O card is not capable of providing enough power to energize the solenoid valves, so a relay circuit [29] is used to allow the weak current from the card to switch the power from an external 12V DC supply (B&K Precision Corporation, Yorba Linda, CA) to the individual solenoids.

The Microfluidic Module (MM) is designed to have a mixing chamber depth of 35 μm. This depth is established by a 35 μm thick, 1 mm wide transparent film (3M, St. Paul, MN) inserted between the top and bottom of the chamber during assembly. A combination of the film and silicon sealant (GE Sealants & Adhesives, Huntersville, NC) formed the walls of the chamber [29]. The bottom of the mixing chamber is a standard 25 X 75 mm microscope slide. The top of the mixing chamber is made from a combination of PDMS and a 50 X 70 mm glass microscope slide. The glass slide has four ports drilled out in the location of the desired sources and sinks (near each corner of

the bottom microscope slide). A 1 mm thick layer of PDMS with 25 μm deep channels, fabricated using soft lithography methods, is plasma-bonded to the top of the 50 X 70 mm glass slide [29]. Each of the channels connects two ports along the long side of the glass slide. In the middle of each channel there is a T-junction that leads upward through a 7.5 mm high, 6 mm diameter cylinder of PDMS that is integrated into the thin layer of PDMS. At these central ports a steel tube is pressed in to act as a plumbing connector to the pumping unit.

The PSSMD chamber is designed to have a volume no greater than 50 μl. The chamber is also designed with minimizing the dead volume of the device in mind, or the volume of fluid that is not available for mixing. In order to minimize dead volume, the channels are made with a depth of 25 μm and a width of 250 μm. The total length of all the channels is 150 mm, which gives us a total dead volume less than 1 μl with in the channels. Considering the volume in the source-sink ports to be dead, in addition to the channels, gives us a total dead volume around 15 μl.

The PSSMD is assembled by placing the MM between two plexi glass plates that are apart of the valving unit superstructure (the solenoids are attached to the top plate) and provide structural integrity to the device. Holes are machined in the top plate to allow for the connection of the plumbing and for access to the channels for the solenoid actuators. Figure 28 is an illustration of this assembly.
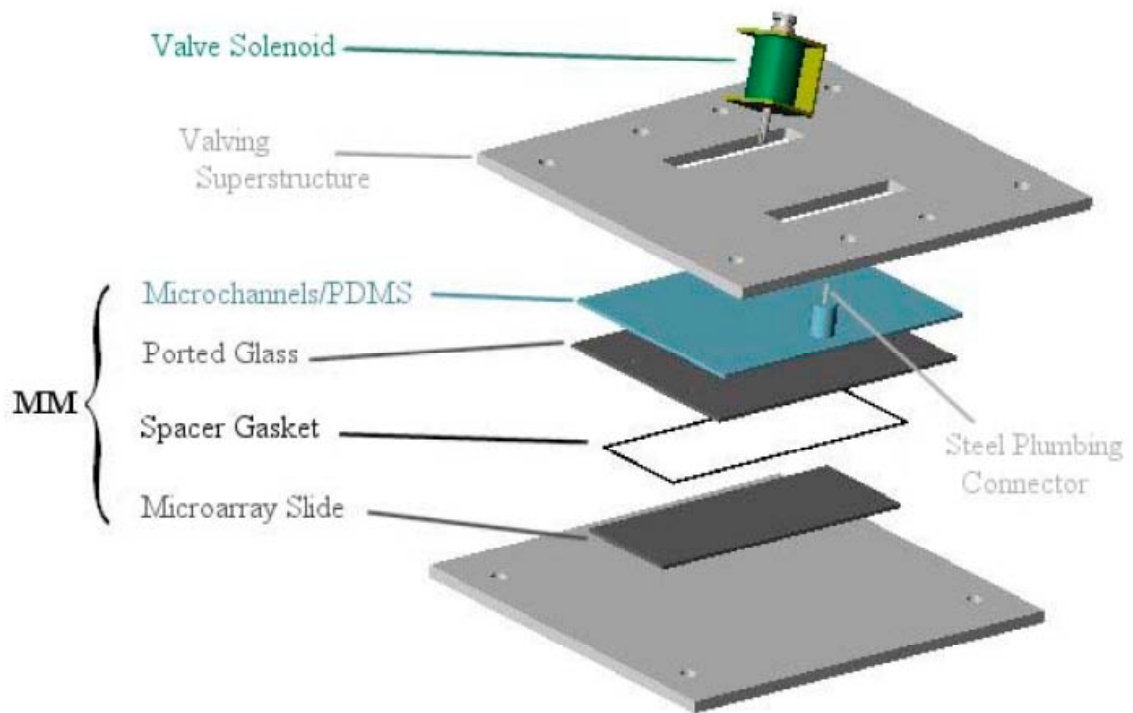
Figure 28. On-board components of the PSSMD [29].

The PSSMD is design so that the mixing chamber is optically clear and is visually unobstructed by any other component of the device. This is done so that mixing test can be done with a dye solution used for visualizing the flow and photos can be taken.

A proof of concept experiment is conducted for the novel PSSMD design [29]. The performance of the components of the PSSMD as well as the mixing ability of the chamber over different pulse volumes is of interest. A dye solution of 0.50% erioglaucine (Sigma Inc., St. Louis, MO) is used to visualize the flow in the experiments. Mixing conditions through a range of pulse volumes from 25% to 100% of the total chamber volume are tested.

To begin each experiment the mixing chamber is filled with a clean solution (ethanol), then a dye solution equal to ten percent of the chamber volume, 5 μl, is injected into the channel that will act as a source for the first half period. The fully assembled PSSMD is placed on a light box, which provides an invariable background of light. The Virtual Instrument in the control unit is then set to a specified pulse volume, and the PSSMD is activated. The device is allowed to run for enough cycles so that it is visually determined that the dye is uniformly distributed.

A high-resolution digital camera (Nikon Corporation, Tokyo, Japan) is used to record images of the chamber before each half-cycle throughout the test. A reference photo is also taken of the chamber, before dye is injected for each run. These images are then used to quantify the mixing ability of the chamber. A bitmap analyses (Image Pro software, Media Cybernetics Inc., Carlsbad, CA) is used to determine individual pixel intensities within a specified region of interest, which is chosen to represent the area that would contain spots of DNA on a microarray. This area is shown boxed of in the image of figure 29.

Figure 29. Area designated for pixel intensity analysis. This area is chosen based of the application of this technology to DNA hybridization [29].

The pixel intensities for each photo are used to calculate a mean and standard deviation for each photo. The coefficient of variation in each image is calculated by dividing the standard deviation by the mean. Back ground interference is factored out using the data from the reference photos. The coefficient of variation pixel intensity data is used to compare the mixing in the case of different pulse volumes [29].

Results From Previous Experiment

The previous experiments provide results that characterize an intermediate trend with respect to mixing over increasing pulse volume [29]. It is stated that as the pulse volume is increased from 25% up to 75% of the total chamber volume the time required to achieve uniform distribution (good mixing) is shortened. Also, that for pulse volumes of 75% up to 100% of the total chamber volume the mixing efficiency slightly decreases. This is stated to be a result of the initial dye stretching toward the perimeter of the chamber, where most of it is not in the boxed mixing area of interest. In the previous work [29] experiments of different pulse volumes have different relaxation times, or time for the flow to come to rest, because the total cycle duration is held constant throughout each experiment; due to this the smaller pulse volumes end up having more rest time than the larger ones. A theoretical correction for this is done giving each test a relaxation time of 20 seconds. Even after this correction the data shows the same trend, which ultimately leads to the conclusion that the larger pulse volumes not only provide better mixing, but they also provide more efficient mixing, and that the most effective pulse volume is 75% of the chamber volume.

Changes Made to Experiment

Mentioned as 'Future Endeavors' in the previous work [29], parts of the PSSMD that is thought to need further refinement are noted; given the novel nature of the design this needed refinement is not unexpected. A need for improved techniques in the fabrication of the source-sink ports is mentioned. The ports make up 93% of the dead volume of the device, and it is desired to make the dead volume as small as possible [29]. The valving apparatus is also mentioned as a potential area of improvement. The current state of the valving system requires an additional power supply and bulky external setup that complicates the assembly of the PSSMD. A finial area of potential improvement deals with the physical dimensioning and structural integrity of the mixing chamber. The previous work points out that while the mixing chamber is designed to contain a set volume of fluid, it proved very difficult to maintain that volume [29]. The work states that because of the large aspect ratio of the chamber it is reasonable to believe that the actual volume in the experiments varied significantly with internal as well as external pressures.

Unlike the previous work [29], which concentrated on the specific application of DNA hybridization, the work of this paper is directed towards characterizing the general mixing behavior of the PSSMD as it may apply to many applications. After consulting the recommendations for improvement in the previous work [29], and with the thought in mind of generally improving the performance and reliability of the PSSMD several changes are made to the PSSMD. The changes are conceptual, structural, material, and procedural in nature.

Two conceptual changes are made to the way the PSSMD is viewed. The first change deals with the definition of dead volume. In the previous work [29] the volume of fluid in the source-sink ports made up 93% of the dead volume of the device and accounted for about 14 μl of fluid volume; because of the large depth of the source-sink ports in relation to the chamber depth (20:1) and the very slow fluid velocity in the chamber, this study will view the 14 μl of dead volume as 'alive and well', and it will be included in the total volume of the mixing chamber. This shift in view will require a correction to be made to how much fluid volume is being pumped into the chamber during a given cycle. The second conceptual change deals with the area of interest for mixing considerations. Since the previous work is only concerned with mixing as it relates to DNA hybridization [29], a boxed off area centered on the chamber is the only area where pixel intensities are examined; the edges of the chamber are left unexamined. This study will measure the pixel intensities and compare intensity coefficient of variations for the entire chamber; including all the way up to the edges.

Two structural changes are made to the PSSMD. Both of the changes made are made with the intention of solving the problems the previous work [29] was having with keeping a constant chamber volume. The changes also allow the chamber to be assembled submerged in a fluid, which eliminates a huge problem of purging the chamber of air bubbles. A brass gasket 50 μm thick (manufactured in the Vanderbilt Machine Shop) is used to provide the depth and wall constitution of the chamber, instead of the thin film and silicon adhesive used before. The plexi glass superstructure of the valving system is replaced with a redesigned brass structure that is capable of applying enough pressure across the MM to sandwich the top and bottom of the MM around the

brass gasket and seal the chamber. The small surface tolerances of the brass gasket and glass slides allows for the creation of a liquid tight seal all around the chamber. An illustration of this assembly is shown in figure 30.
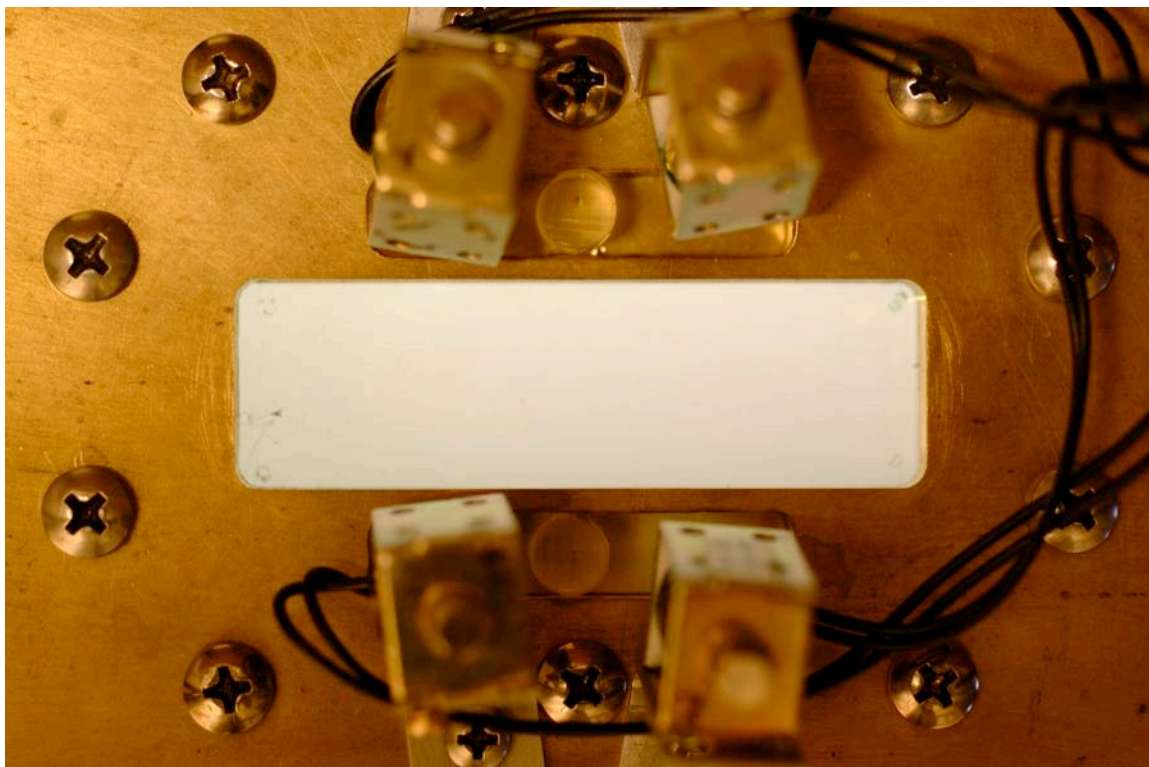
Figure 30. Photo of the new Microfluidic Module fully assembled.

Two material changes are made to the operation of the PSSMD. A dye solution of 10% eiroglucine is used instead of a 0.5 % solution. This is done in hope of getting a more easily read signal and a better overall visualization of the flow. Water is used as the blank solution in the chamber, and the dye solution is also water based. In the previous work [29] ethanol is used as the blank solution, and the dye is water based; which might have caused some fluid interfacial behaviors that affect the flow. A water-water setup for

51

the 50% case is used in the previous work to test the validity of the trends shown in the ethanol-water test [29]. Based off the water-water 50% test it looks as if the trends are the same. The fact that the previous work only ran one water-water case gives more weight to reexamining the behavior of this system.

Three procedural changes are made to the parameters of the PSSMD experiment. Since the new brass gasket changes the depth of the chamber from 35 μm to 50 μm, and the liquid in the source-sink ports is to be counted as part of the chamber volume (all the ports will be considered 'alive and well' for this study, but future work requires further examination of this), the chambers volume changes from 50 μl to 90 μl. To account for this an extra 5 μl of dye is injected in to the chamber. The way the dye is initially injected into the chamber is also changed. Before, the experiment is setup so that the dye begins entering the chamber at the source during the first half cycle [29]. This procedure is changed so that the mixing chamber starts out with a similar initial blob of dye, located at the first half-cycle source, for each case. The other change made is to the amount of relaxation time during a half cycle. The amount of relaxation time during previous experiments [29] is allowed to change with different pulse volumes; it will be held constant at 30 seconds during current test.

New Experimental Setup and Procedure

This section presents the setup, procedure, and results of the current experiments. The focus of these experiments is to help characterize the mixing behavior of a 21 X 71 X 0.05 mm chamber that is subjected to pulsed source-sink induced chaotic advection over a range of pulse volumes. The pulse volumes that are examined in this experiment are

5%, 25%, 42.5%, 50%, 60%, 75%, and 100% of the total chamber volume. The total

chamber volume is defined to be the chamber volume plus the volume of the source-sink

ports in the roof of the chamber, which comes out to be about 90 µl.

The experimental setup of the PSSMD [29] consists of four components: Control

Unit, Pumping Unit, Valving Unit, and Microfluidic Module. The control unit runs the

pumping and valving units that are both connected to the MM as show in figure 31 (for a

schematic of this assembly refer to figures 27).
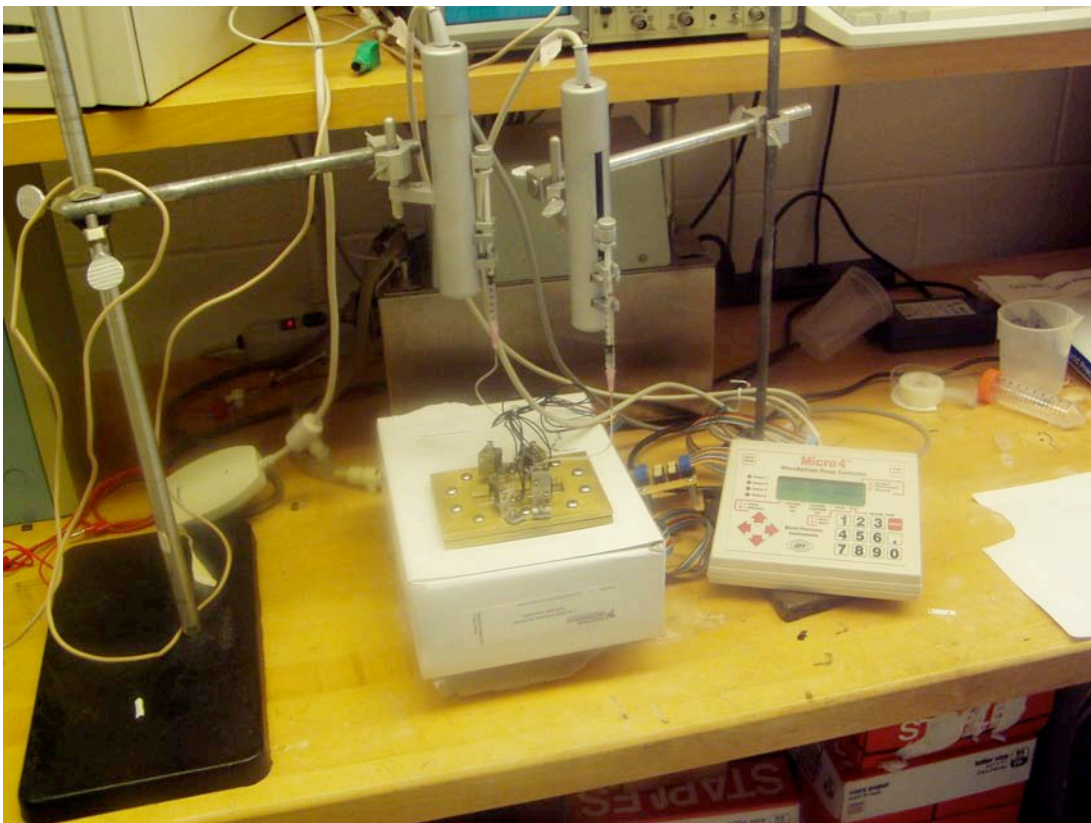
Figure 31. Photo of lab setup.

To begin each experiment the 500 µl syringes and vinyl tubing of the pumping unit are filled with water. This is done under water to prevent bubbles from appearing in the syringes or tubing (the syringes can be detached and reattached to the unit easily). Next the components of the MM and valving superstructure are submerged in water and assembled. Special attention is made to tighten down (the top glass slide will break if too much pressure is applied; due to small surface tolerances in relation to the chamber depth a small amount of pressure is sufficient to seal the chamber) the valving superstructure around the MM just enough to provide adequate force to seal the top and bottom glass slides around the brass gasket, in effect creating a sealed mixing chamber. This method of assembly easily keeps the mixing chamber free of bubbles. The MM, secured by the valving superstructure, is dried off with a paper towel then placed on a light box. The solenoid actuators are connected to the top of the valving superstructure and the tips of the solenoids are lined up over there respective microchannels, so that when actuated they will effectively pinch off the channel. The vinyl tube coming off one of the syringes of the pumping unit is attached to the side of the MM where a sink will be activated during the first half-cycle of operation. This connection is made through a 20 gauge steel tube that has been inserted in the end of the vinyl tube and is now inserted into the cylinder of PDMS that leads down to the microchannels. In order to prevent bubbles from entering the system it is important to form a meniscus at the tip of the steel tube and the top of the PDMS cylinder before joining the two. At this point the lights in the room are turned off, the light box is turned on, and a reference photo is taken, using a Nikon High resolution digital camera set on a tripod and positioned directly over the MM's mixing chamber, of the dye free chamber. This photo is taken for each test run and is used to identify and

deal with background interference. Now, on the side of the MM where a source will be on during the first half-cycle of operation, a 15 μl (in reality this varied between 10 μl and 15 μl throughout different runs because of the difficulty involved with getting an exact amount of dye into the chamber; corrections will be made for this in analyzing results) blob of 10% erioglucine dye solution is inserted into the chamber at the source location. This is done by manually pinching off the side of the microchannel opposite of the first half-cycle source, and inserting the dye using a 20 gauge blunt needle and a syringe full of the dye solution. After the blob of dye is successfully inserted, and while keeping the microchannel opposite of the first half-cycle source pinched off, the vinyl tube coming from the other syringe of the pumping system is connected to the MM exactly as it was done with the first tube.

Once the four components of the PSSMD are assembled, attention is turned to setting the operating parameters on the VI of the control unit. The flow rate is chosen to be 3 μl/s (same as in [29]), which gives the flow a Reynolds number of about 20 when entering the chamber from the microchannels, assuring laminar behavior. This Reynolds number calculation is shown below in equation 14.

For water: $\nu := 1.12 \cdot 10^{-6} \quad \dfrac{m^2}{s}$

Hydrolic diameter of microchannel: $D_h := .0458 \quad mm$

Flow rate: $q = 3 \quad \dfrac{\mu l}{s}$ or $q := 3 \quad \dfrac{mm^3}{s}$

Cross sectional area of microchannel: $A := 6.25 \times 10^{-3} \quad mm^2$

Flow velocity: $V := \dfrac{q}{A} \qquad V = 480 \quad \dfrac{mm}{s}$

Reynolds Number: $Re := \dfrac{V \cdot D_h}{\nu \cdot 1000^2} \qquad Re = 19.629$ (14)

The time for allowing the fluid to relax during a given half-cycle is set to 30 seconds and is held constant for every run. The delay, or time before the next half-cycle that the solenoids switch changing the source and sink that are on, is set to 2 seconds and is held constant for every run. This means that 2 seconds before the end of the relaxation time for a given half-cycle the sources and sinks switch to get ready for the next half-cycle. The volume of fluid being pulsed and the total amount of time for a half-cycle of operation varies with different runs. The table of figure 32 shows the Virtual Instrument controlled system parameters for each test conducted in this study.

% Chamber Volume	Flow Volume (nl)	Flow Rate (nl/s)	Time of Source-Sink Operation During Cycle (s)	Relaxation Time (s)	Total Time of One Cycle (s)	Delay (s)
5	4500	3000	1.5	30	31.5	2
25	22500	3000	7.5	30	37.5	2
42.5	38250	3000	12.75	30	42.75	2
50	45000	3000	15	30	45	2
60	54000	3000	18	30	48	2
75	67500	3000	22.5	30	52.5	2
100	90000	3000	30	30	60	2

Figure 32. These are the test conditions of each pulse volume case. The flow volume and time of source-sink operation changes for each case. The flow rate is held constant throughout the experiments. The relaxation time is the time between when the flow stops and the beginning of the next cycle. The total time of one cycle is the sum of the relaxation time and the time of source-sink operation. The delay is equal to the amount of time before the next cycle that the solenoids switch activation; placing the other source and sink ready for operation.

Before running a test a photo is taken of the mixing chamber with the initial blob of dye.

This initial condition is shown in figure 33.

Figure 33. This is an example of what it looks like when the mixing chamber is setup before each experiment with an initial blob of dye. The dye is inserted at the location of the source to be on during the first half-cycle of operation.

When the test is set to run, and begins running, a photo is taken after every half-cycle for the first 15 full-cycles. At this point subsequent photos are taken at the end of every 5th full-cycle. Ideally the test would be allowed to run until the dye visually appears uniformly distributed throughout the chamber, but in reality some test were stopped because of air bubbles appearing in the chamber after awhile. It was found that the longer the test runs, the more likely it was for an air bubble to eventually penetrate the chamber. This air bubble problem affected the lower pulse volume test the most, as will be explained in the results of this section.

Results From New Experiment

Test are run with the PSSMD for pulse volumes set to 5%, 25%, 42.5%, 50%, 60%, 75%, and 100% of the total chamber volume. A few test are run for each pulse volume case and the results herein are a best representation of the gathered data. The experimental results afford us two ways of analyzing the mixing capabilities of the PSSMD. The first, and most obvious way is by simply making a visual analysis. Visual analysis is crude and hard to quantify, but it can be worthwhile by providing extra insight into fluid behavior. The second way to analyze the experimental results is by examining the pixel intensities of the photos taken during the runs. The bulk of the analysis done in this study involves this second method; which is less crude and can provide a more reliable analysis.

The visual observations of the experimental results are divided into three categories: Low pulse volume observations, middle pulse volume observations, and high

pulse volume observations. Low pulse volumes for this experiment are defined as the 5%

and 25% cases. In both of these cases the initial dye blob has a tendency to stay on one

side of the mixing chamber as shown in the sequence of photos for the 25% case in figure

34.

Figure 34. The sequence of photos is from when 25% of the chambers volume is pulsed. (a) is the mixing chamber, with the initial blob of dye, before the PSSMD is put into operation. (b) is the mixing chamber after 1 full cycle of operation, (c) is the mixing chamber after 3 full cycles, (d) is the mixing chamber after 5 full cycles, (e) is the mixing chamber after 7 full cycles, and (f) is the mixing chamber after 9 full cycles. It is noted that photos (b) to (f) show the dye's tendency to stay to one side of the mixing chamber.

Middle pulse volumes for this experiment are defined as the 42.5%, 50%, and 60% cases.

These cases are characterized by the initial dye blob sweeping down the center of the

mixing chamber with a parabolic looking trajectory. For the 42.5% case the bottom tail

of the parabolic trajectory ends up being located at the source (slightly to the inside, this

is important because if it were to the outside, as shown in figure 36(b), it would get push

into the wall of the chamber when the source is activated, as shown in figure 36(c), instead of back towards the middle of the mixing chamber) to be activated in the second half-cycle of operation; this is illustrated in figure 35(b). This is noted, because on the second half-cycle stroke, figure 35(c), the bit of 'tail' dye is pulsed out in a parabolic looking trajectory towards the middle of the mixing chamber and is distributed more uniformly. The behavior of the middle cases, represented by the 42.5% case, is displayed in the sequence of photos in figure 35.
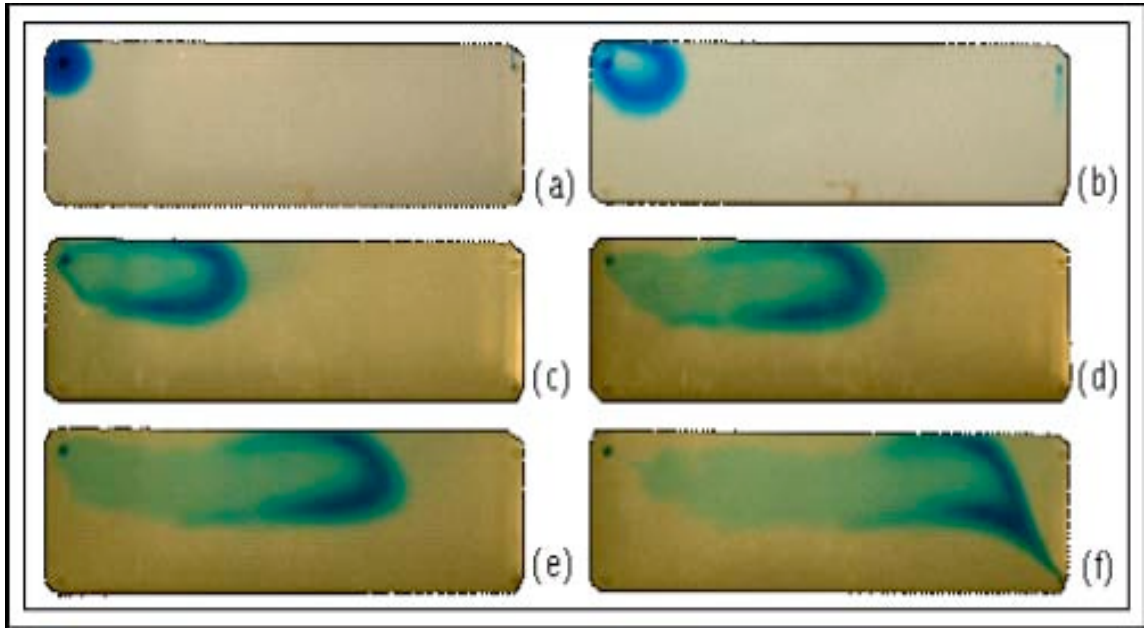

Figure 35. The sequence of photos is from when 42.5% of the chambers volume is pulsed. (a) is the mixing chamber, with the initial blob of dye, before the PSSMD is put into operation. (b) is the mixing chamber after 1 half cycle of operation, (c) is the mixing chamber after 1 full cycle, (d) is the mixing chamber after 2 full cycles, (e) is the mixing chamber after 3 full cycles, (f) is the mixing chamber after 4 half cycles, and (g) is the mixing chamber after 4 full cycles. It is noted that photos (b) to (g) show the dye traveling down the middle of the mixing chamber and being dispersed more rapidly due to the 'tail' dye located as shown in (b).

High pulse volumes for this experiment are defined as the 75% and 100% cases. The

75% case behaves different enough from the 100% case to warrant not talking about them

as one group. In the 75% case the initial dye blob transverses the mixing chamber with

parabolic looking motion similar to the middle observations, although the dye is pushed

close to the walls. Unlike the middle pulse volumes where there is some dye slightly to

the inside of the source to be activated on the second half-cycle, the 75% case left dye

slightly to the outside, as shown in figure 36(b), of the source (closer to the walls of the

mixing chamber). When the second half-cycle is activated the dye gets push even further

up against the wall, as shown in figure 36(c). This behavior is fully illustrated by the

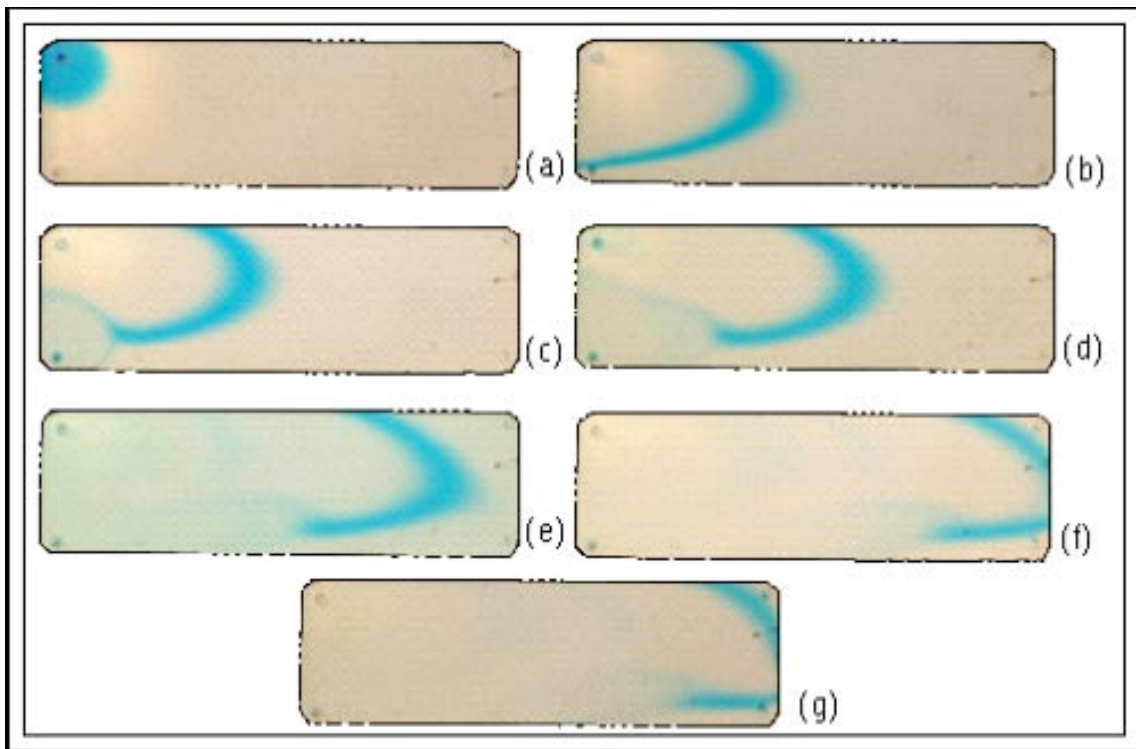sequence of photos in figure 36.
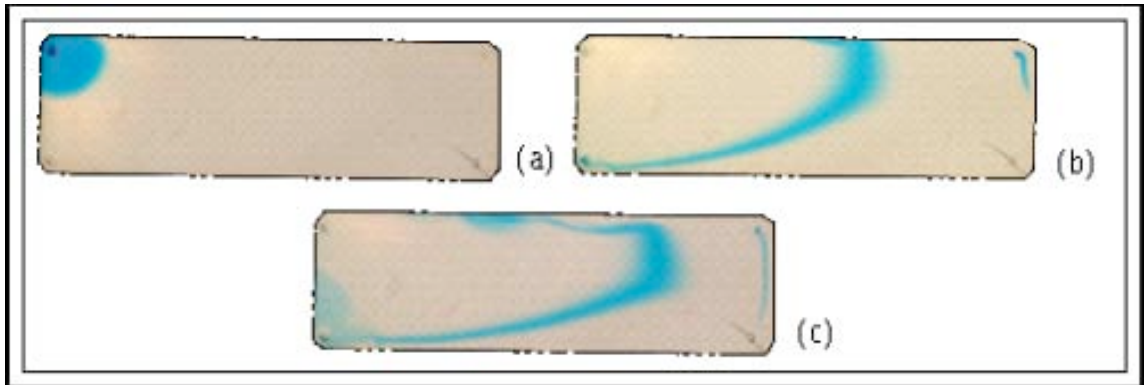
Figure 36. The sequence of photos is from when 75% of the chambers volume is pulsed. (a) is the mixing chamber, with the initial blob of dye, before the PSSMD is put into operation. (b) is the mixing chamber after 1 half cycle of operation and (c) is the mixing chamber after 1 full cycle of operation. It is noted that photos (b) and (c) show the tendency for the dye to get pushed up against the walls of the mixing chamber (although not as much as the 100% case illustrated in figure 37).

In the 100% case the initial blob of dye completely travels the length of the mixing

chamber as illustrated in figure 37(b). While traveling the length of the chamber the dye

61

is pushed close to the walls of the chamber. This trend of being pushed close to the walls is noticed throughout the 100% cases. Even after several cycles it can be observed that dye is accumulating near the sides of the mixing chamber, as illustrated in figure 38. The photos in figures 37 and figures 38 illustrate this concept.
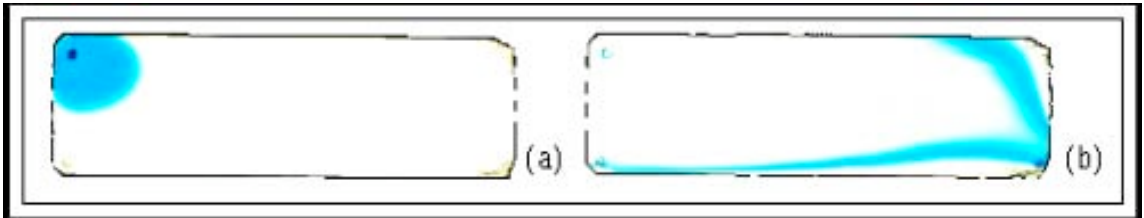
Figure 37. The two photos are from when 100% of the chambers volume is pulsed (different lighting was used in this particular run). (a) is the mixing chamber, with the initial blob of dye, before the PSSMD is put into operation and (b) is the mixing chamber after 1 half cycle of operation. It is noted that the dye transverses the entire chamber during the first half cycle.
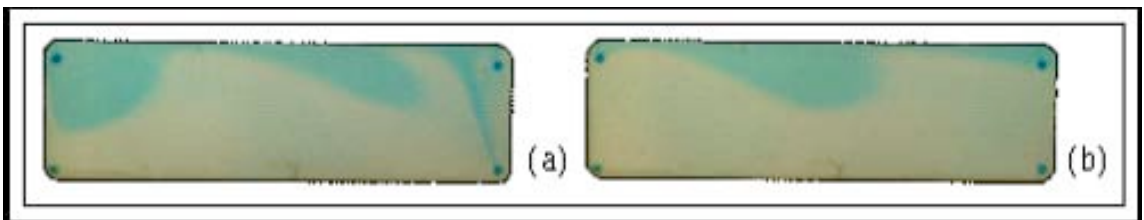
Figure 38. The two photos are from when 100% of the chambers volume is pulsed. (a) is the mixing chamber after 10 half cycles of operation and (b) is the mixing chamber after 10 full cycles of operation. It is noted that the dye is more concentrated near the top wall of the mixing chamber in a pattern that inverts from the half period to the full period.

The pixel intensities of the photos taken during this experiment are used to compare variation across the surface over time for different pulse volume cases. ImageJ, a free program provided by the National Institute of Health (www.nih.gov), is used to extract pixel intensity data from the experimental photos. The pixel intensities are given by the

program on a grey scale. The experimental photos are in color, so ImageJ converts the pixel intensities to a grey scale by taking a weighted average of the reds, blues, and greens in the images. For each photo analyzed using ImageJ the average pixel intensity and the standard deviation of pixel intensities across the chamber are given. This data is used to calculate a pixel intensity coefficient of variation. After accounting for background variation (noise), this coefficient of variation is used as a measure of mixing in our experiment. Smaller coefficients of variation are considered indicators of good mixing, and larger coefficients of variation are considered indicators of poor mixing.

The coefficient of variation is calculated by dividing the standard deviation by the mean. To account for noise in this experiment and to best compare the data extracted with ImageJ this simple calculation requires some manipulation. Equations 15 through 20 show the steps taken to arrive at a meaningful coefficient of variation and equation 21 shows the associated error. Pixel intensities from the reference, or base, photo are denoted as b, while pixel intensities from the image being analyzed is denoted with an I.

I and b can be represented as having the same mean by scaling the I and b means by constants as shown below.

$$c_1 \cdot \bar{I} = \bar{A} \qquad\qquad c_2 \cdot \bar{b} = \bar{A} \tag{15},(16)$$

It can be shown from equations (15) and (16) that:

$$\frac{c_1}{c_2} = \frac{\bar{b}}{\bar{I}} \tag{17}$$

The coefficent of variation is now:

$$\text{cov} = \frac{1}{\bar{I}} \cdot \sqrt{\frac{\sum\limits_N (I - \bar{A})^2}{N}} - \frac{1}{\bar{b}} \cdot \sqrt{\frac{\sum\limits_N (b - \bar{A})^2}{N}} \tag{18}$$

By substituting for A, expanding the summation, and using some simple algebra the cov can be represented as:

$$\text{cov} = \frac{c_1}{c_2 \bar{I}} \cdot \sqrt{\frac{\sum\limits_N \frac{1}{c_1{}^2}(I - c_1 \cdot \bar{I})^2}{N}} - \frac{1}{\bar{b}} \cdot \sqrt{\frac{\sum\limits_N \frac{1}{c_2{}^2}(b - c_2 \cdot \bar{b})^2}{N}} \tag{19}$$

To get a relation using the data available from ImageJ cov is approximated with:

$$\text{cov} = \frac{c_1}{c_2 \bar{I}} \cdot \sqrt{\frac{\sum\limits_N (I - \bar{I})^2}{N}} - \frac{1}{\bar{b}} \cdot \sqrt{\frac{\sum\limits_N (b - \bar{b})^2}{N}} \tag{20}$$

The error associated with is approximation is about

$$\text{error} = (c_1 - c_2)^2 \tag{21}$$

Error was usually on the order of 0.01. The actual coefficient of variation is now shown as a scaling constant times the image coefficient of variation minus the base coefficient of variation. To better graphically compare actual coefficients of variation from different test runs, which might have different base coefficients of variation, the actual coefficients of variation are scaled so that each base coefficient of variation has a value that is equal to 0.1.

Figure 39 shows a comparison of how the pixel intensity coefficient of variation changes over time for different percentages of the total chamber volume pulsed into the chamber during a half-cycle. On the chart the base value of 0.1 is noted with a black line, this value is considered to be the state of 'perfectly uniform' distribution, or perfect, mixing. At time zero each case starts with an initial variation that is based on the dye blob that was injected in the chamber. This initial point is seen as varying because in reality the dye blob is not always the same shape, and the dye concentration of the blob sometimes varies. While pointed out, these initial condition discrepancies have little effect on the trends shown by the data.
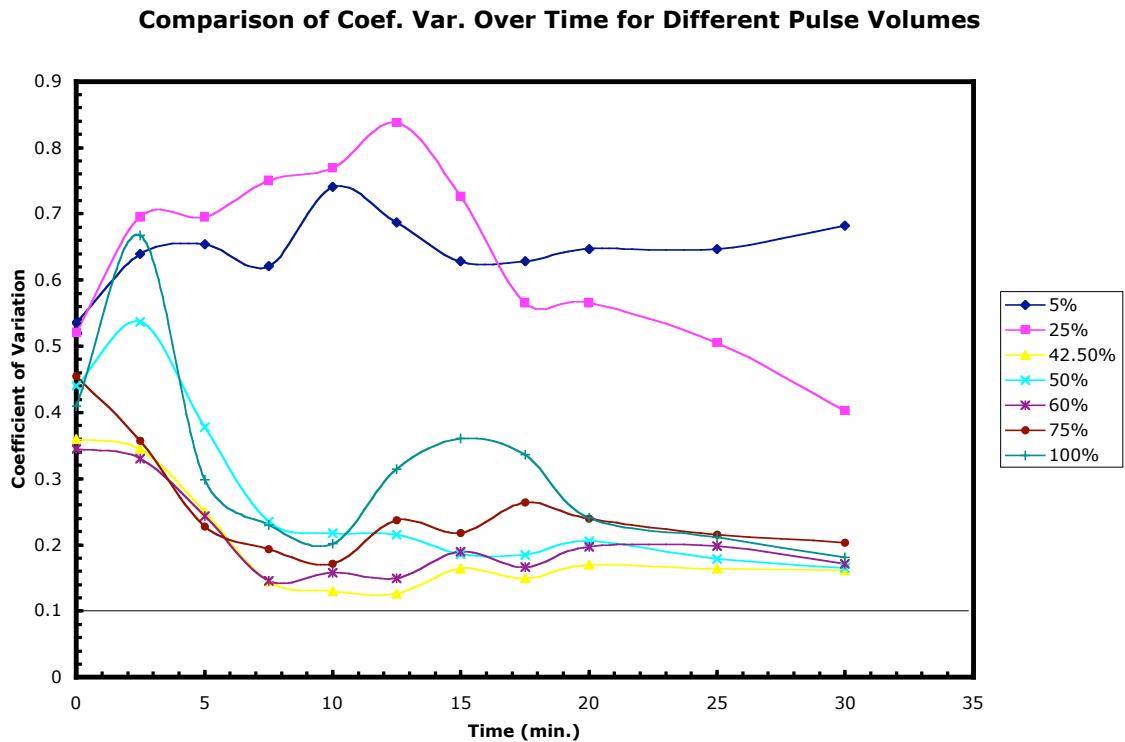

Figure 39. Plot of coefficient of variance over time for all pulse volumes.

It is noted from figure 39 that the lower pulsed volumes of 5% and 25% of the total chamber volume provide a varied distribution, far from uniform. The most uniform distribution is achieved at a pulse volume equal to 42.5% of the total chamber volume. As the pulse volume is increased from 42.5% to 100% the variedness of the distributions increases slightly with increasing pulse volume. Because of error associated with the calculation of the coefficients of variation, it is safe to say that after 30 minutes the differences in the coefficient of variation for the 42.5%, 50%, 60%, 75%, and 100% cases, while there, are small.

Figure 39 shows coefficient of variation as it changes over time, but it is also important to look at how the coefficient of variation changes over number of cycles. The more cycles it takes to reach a uniform distribution, the less efficient the mixing. This is easily understood by thinking of additional cycles as additional work being put into the system; if the output is the same (similar or better mixing) then the process is less efficient. In figure 39 the data is presented on a 30 minute time scale. In these 30 minutes each pulse volume case goes through a different number of pulse cycles. The general relation is the larger the pulse volume the more time it takes to pulse, and therefore that test goes through less cycles than a smaller pulsed volume for a given duration of time. Figures 40, 41, and 42 show a comparison of coefficient of variation for the test range of pulse volumes after 5, 10, and 15 full-cycles (30 half-cycles). The 5% and 25% cases give a relatively high coefficient of variation and are very inefficient in doing so. The 75% and 100% cases give coefficients of variation that are similar to the 42.5%, 50%, and 60% cases, but are slightly less efficient in doing so. As it turns out the

cases of 42.5%, 50%, and 60% of the total chamber volume pulsed not only provide the

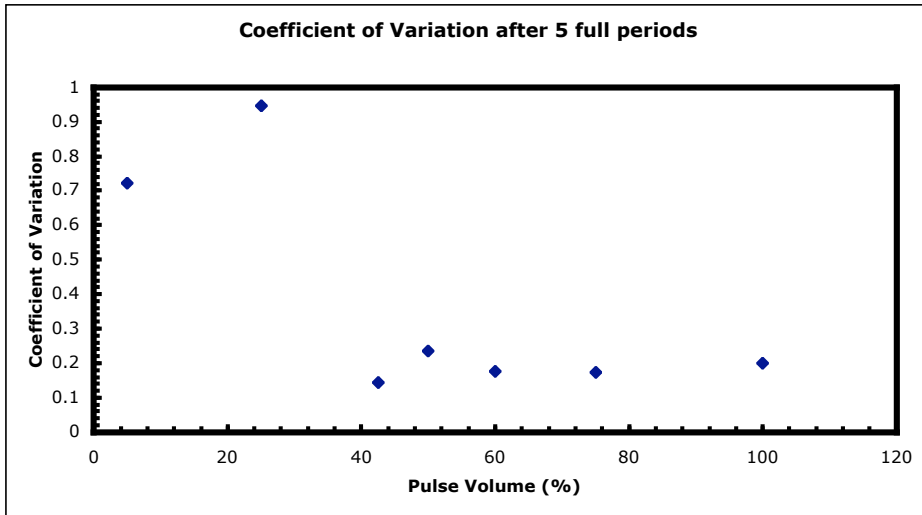lowest coefficients of variation, but they are also the most efficient at doing so.

Figure 40. Plot of the coefficient of variance for all pulse volumes, after 5 full periods.
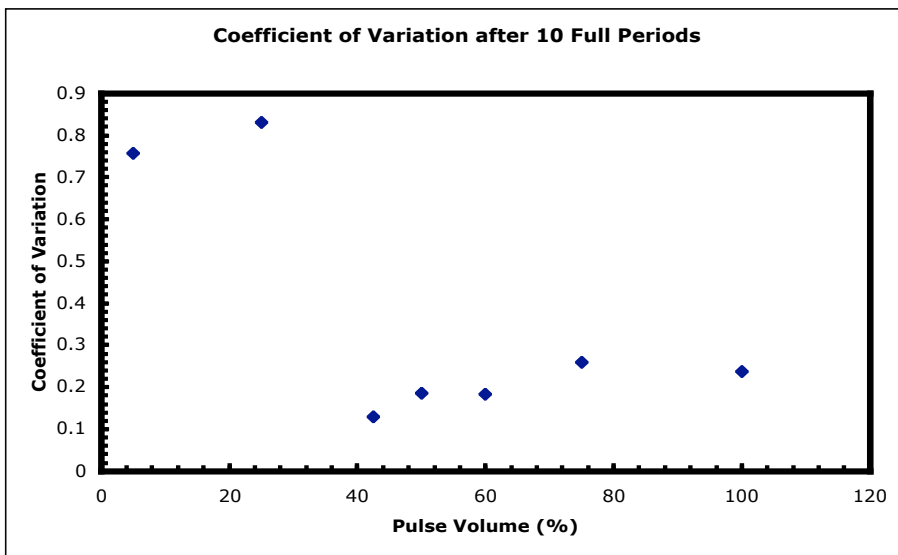
Figure 41. Plot of the coefficient of variance for all pulse volumes, after 10 full periods.
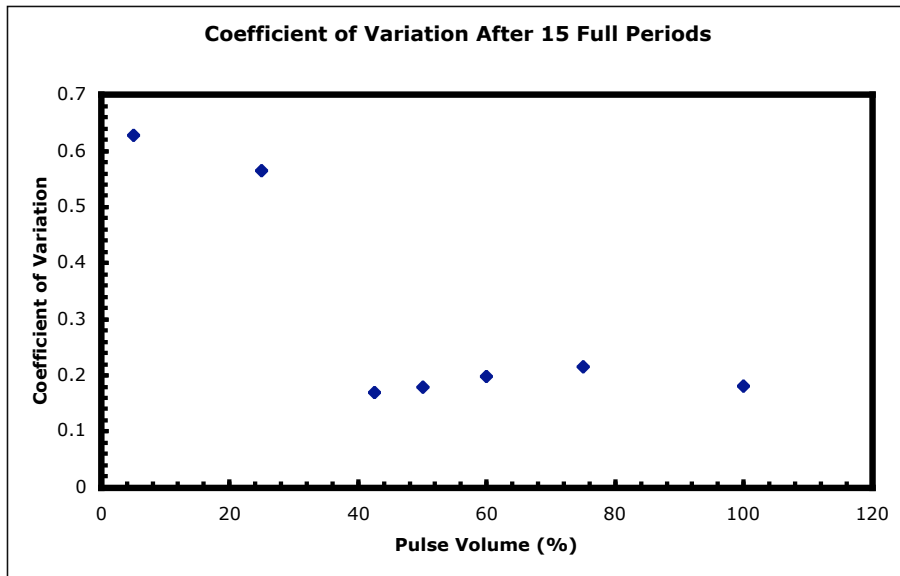
Figure 42. Plot of the coefficient of variance for all pulse volumes, after 15 full periods.

To better compare the experimental results to the numerical work done in Chapter II the pixel intensity coefficients of variation comparisons for the test cases are repotted in figure 43 subtracting out the standard relaxation time of 30 seconds (in reality it is not practical to be able to switch between half-cycles without some amount of delay, so this could not be done experimentally). A difference worth pointing out on this new plot is the lower coefficients of variation shown for the 5% and 25% cases. The subtraction of the 30 seconds relaxation time allowed these cases in particular to go through a lot more cycles than what was displayed before. So while the mixing looks better in these cases, they are still very inefficient.

Comparison of Coef. Var. over time for different Pulse Volumes (adjusted)
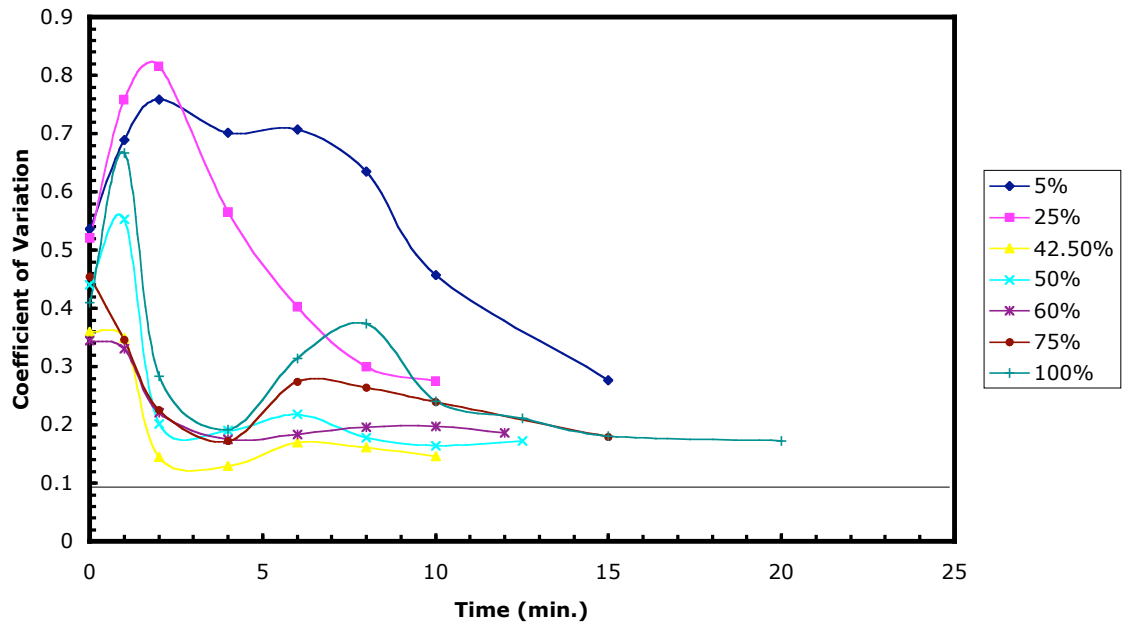
Figure 43. Plot of coefficient of variance over time for all pulse volumes; adjusted to factor out the relaxation time.

Comparison of Old and New Experimental Results

The biggest change in comparing the work done in this study to the work previously done [29] is probably the way the total chamber volume is considered. This study considers the total chamber volume to include the volume contained in the source-sink ports on the top glass slide of the MM. The previous work did not consider this part of the chamber volume; it classified that volume as dead [29]. If the previous work included the extra volume as it is done in this study, then the total volume used in the previous experiments would increase by 30% (the volume in this study is increased by only 20% by the addition of the source-sink port volume; this is due to the larger mixing chamber size in this study). This increase in chamber volume would skew the numbers from the previous

work [29], causing them to better match the data presented in this study. The previous work's best mixing value of 75% of the total chamber volume being pulsed [29] would change to 58% of the total chamber volume being pulsed. In the previous work keeping a set chamber volume is found to be difficult in general, due to the lack of sufficient structural integrity in the setup. Another significant change to examine is the area of the chamber considered when examining pixel intensities. In this study pixel intensities across the entire mixing chamber are examined. In the previous work only pixels that were within a certain boxed off middle area are examined (see figure 29), which eliminates analysis of behaviors close to the walls of the mixing chamber. After considering the conceptual differences between this study and the previous work, it is possible to conclude that the trends seen in both studies relate, and data pertinent to the behavioral characterization of the mixing chamber, as the pulse volume is changed, can be drawn from both studies.

Experimental Study vs. Numerical Study

The effective Reynolds number of the flow inside the mixing chamber is about 0.15. In the numerical model the flow in side the mixing chamber is modeled as a Hele-Shaw flow where the flow is defined as having a Reynolds number much less than 1, Re << 1. While 0.15 may not be considered much less than 1, it is still small enough to validate the numerical assumption. The numerical model uses a depth-averaged velocity, which allows for a potential flow assumption. This assumption is validated by the small depth (50 μm) and large aspect ratio of the mixing chamber. The finial big assumption in the numerical model deals with how the fluid is reinjected into the chamber. A 'last in-first

out' method is used throughout the numerical work, which is a good representation of what happens in reality, but the angle at which a fluid particle re-enters the chamber is changed between being a 'remembered angle' (as calculated in the Poincaré maps) and a random angle (as calculated in the stochastic analysis). It is thought that during the real experiments the reentry angle is somewhere between 'remembered' and random.

CHAPTER V

DISCUSION

Conclusion

With the rapid advancement of technology in today's world it is important to pursue undertakings that help to meet the unavoidable challenges that no doubt will arise. The focus of this study is set forth to meet such a challenge. The goal of this study is to characterize the mixing within a rectangular chamber that is part of a pulsed source-sink mixing device; by pulsing source-sink pairs, chaotic advection was produced within the chamber to motivate the flow. In pursuant of this goal a range of pulse volumes, which made up a set percent of the total chamber volume, is studied in operation of the PSSMD and in a numerical analysis.

The PSSMD experiment as previously setup [29] is modified to produce a more stable device that is easier to use. The experimental procedure and concepts are also modified in attempt to get a better characterization of the mixing in the device. Several experiments are run with the PSSMD using different pulse volumes. The middle range, about 40% to 60% of the total chamber volume, of pulse volumes shows the most optimal mixing.

By making a few simple assumptions a numerical model is made to study the chaos, potential mixing, in the PSSMD. The numerical results show the potential for optimal mixing in the middle range, 39% to 45% of the total chamber volume pulsed. In the lower range the numerical results hint at the possibility of optimal mixing in special applications.

As it turns out there is good agreement between the numerical results and the experimental ones. Both studies classify a middle region of pulse volumes, of similar magnitude that produced indications of optimal mixing. In both studies, when the pulse volume is set in a range between about 75% and 100% of the total chamber volume the mixing is less optimal than in the middle pulse volume range. In the range of lower pulse volumes (about 5% to 30% of total chamber volume) the two studies show varying results; the numerical results show some potential for optimal mixing in this range for certain applications, while the experimental results show poor mixing in this range.

Future Work

This study only serves as a beginning to understanding the mixing behavior in pulsed source-sink systems. In this study the only parameter that is varied in the system is pulse volume; there are several other parameters that can be varied and studied in a pulsed source-sink system like boundary shape, number of sources and sinks, source-sink location, and reinjection method.

As with any experimentation, additional work can be done to refine the experimental equipment and techniques. Particular focus should be applied to making the PSSMD self contained and easier to manufacture and assemble.

REFERENCES

[1] J. M. Ottino, "Mixing, Chaotic Advection, and Turbulence," *Annu. Rev. Fluid Mech.* **22**, 207-253 (1990).

[2] Chih-Ming Ho, "Fluidics –The Link Between Micro and Nano Sciences and Technologies," *IEEE* 375-384 (2001).

[3] Mark A. Stremler, F. R. Haselton & Hassan Aref, "Designing for chaos: Applications of chaotic advection at the microscale," *Philosophical Transactions of the Royal Society, London, Series A*, to appear.

[4] Abraham D. Stroock, Stephan K.W. Dertinger, Armand Ajdari, Igor Mezic, Howard A. Stone, George M. Whitesides, "Chaotic Mixer for Microchannels," *Science*, Vol **295**, 647-651 (2002).

[5] H. Aref, "Stirring by chaotic advection," *J. Fluid Mech.* **143**, 1-21 (1984).

[6] D. D. Cunningham, "Fluidics and sample handling in clinical chemical analysis," *Anal. Chim. Acta* **429**, 1-18 (2001).

[7] M. Kakuta, F. Bessoth & A. Manz, "Microfabricated devices for fluid mixing and their application for chemical synthesis," *Chem. Rec.* **1**, 395-405 (2001).

[8] D. J. Beebe, G. A. Mensing & G. M. Walker, "Physics and applications of microfluidics in biology," *Ann. Rev. Biomed. Eng.* **4**, 261-286 (2002).

[9] T. Chovan & A. Guttman, "Microfabricated devices in biotechnology and biochemical processing," *Trends Biotech.* **20**(3), 116-122 (2002).

[10] D. R. Meldrum & M. R. Holl, "Microscale bioanalytical systems," *Science 297*, 1197-1198 (2002).

[11] T. H. Schulte, R. L. Bardell & B. H. Weigl, "Microfluidic technologies in clinical diagnostics," *Clin. Chim. Acta 32***1**, 1-10 (2002).

[12] K. Sato, A. Tokeshi, M. Hisamoto & T. Kitamori, "Microchip-based chemical and biochemical analysis systems," *Adv. Drug Deliv. Rev.* **55**, 379-391 (2003).

[13] B. H. Weigl, R. L. Bardell & C. R. Cabrera, "Lab-on-a-chip for drug development," *Adv. Drug Deliv. Rev.* **55**, 349-377 (2003).

[14] S. C. Terry, J. H. Jerman & J. B. Angell, "A Gas Chromatographic Air Analyzer Fabricated on a Silicon Wafer," *IEEE Transactions on Electron Devices*, **26**, 1880-1886 (1979).

[15] A. Manz, N. Graber & H. M. Widmer, "Miniaturized Total Chemical-Analysis Systems – a Novel Concept for Chemical Sensing," *Sensors and Actuators B-Chemical*, **1**(1-6), 244-248 (1990).

[16] C. S. Bangur, A. Switzer, L. Fan, M. J. Marton, M. R. Meyer & T. Wang, "Identification of genes over-expressed in small cell lung carcinoma using suppression subtractive hybridization and cDNA microarray expression analysis," *Oncogene*, **21**(23), 3814-3825 (2002).

[17] V. Brown, P. Jin, S. Ceman, J. C. Darnell, W. T. O'Donnell, S. A. Tenenbaum, X. Jin, Y. Feng, K. D. Wilkinson, J. D. Keene, R. B. Darnell & S. T. Warren, "Microarray identification of FMRP-associated brain mRNAs and altered mRNA translational profiles in fragile X syndrome," *Cell*, **107**(4), 477-87 (2001).

[18] V. Chizhikov, M. Wagner, A. Ivshina, Y. Hoshino, A. Z. Kapikian & K. Chumakov, "Detection and genotyping of human group A rotaviruses by oligonucleotide microarray hybridization," *J Clin Microbiol*, **40**(7), 2398-2407 (2002).

[19] C. Debouck & P. N. Goodfellow, "DNA microarrays in drug discovery and development," *Nat Genet*, **21**(1 Suppl), 48-50 (1999).

[20] H. L. Fredrickson, E. J. Perkins, T. S. Bridges, R. J. Tonucci, J. K. Fleming, A. Nagel, K. Diedrich, A. Mendez-Tenorio, M. J. Doktycz & K. L. Beattie, " Towards environmental toxicogenomics – development of a flow-through, high-density DNA hybridization array and its application to ecotoxicity assessment," *Sci Total Environ*, **274**(1-3), 137-149 (2001).

[21] R. A. Heller, M. Schena, A. Chai, D. Shalon, T. Bedilion, J. Gilmore, D. E. Woolley & R. W. Davis, "Discovery and analysis of inflammatory disease-related genes using cDNA microarrays," *Proc Natl Acad Sci USA*, **94**(6), 2150-2155 (1997).

[22] D. A. Lashkari, J. L. DeRisi, McCusker, A. F. Namath, C. Gentile, S. Y. Hwang, P. O. Brown & R. W. Davis, "Yeast microarrays for genome wide parallel genetic and gene expression analysis," *Proc Natl Acad Sci USA*, **94**(24), 13057-13062 (1997).

[23] L. McNally, M. Baird, K. McElfresh, A. Eisenberg & I. Balazs, "Increased migration rate observed in DNA from evidentiary material precludes the use of sample mixing to resolve forensic case of identity," *Appl Theor Electrophor*, **1**(5), 267-272 (1990).

[24] M. Schena, R. A. Heller, T. P. Theriault, K. Konrad, E. Lachenmeier & R. W. Davis, "Microarrays: biotechnology's discovery platform for functional genomics," *Trends in Biotechnology*, **16**(7), 301-306 (1998).

[25] J. L. DeRisi & V. R. Iyer, "Genomics and array technology," *Curr. Opin. Oncol.* **11**, 76-79 (1999).

[26] A. Watson, A. Mazumder, M. Stewart & S. Balasubramanian, "Technology for microarray analysis of gene expression," *Curr Opin Biotechnol*, **9**(6), 609-614 (1998).

[27] N. B. Adey, M. Lei, M. T. Howard, J. D. Jensen, D. A. Mayo, D. L. Butel, S. C. Coffin, T. C. Moyer, D. E. Slade, M. K. Spute, A. M. Hancock, G. T. Eisenhoffer, B. K. Dalley & M. R. McNeely, "Gains in sensitivity with a device that mixes microarray hybridization solution in a 25-mu m-think chamber," *Analytical Chemistry*, **74**(24), 6413-6417 (2002).

[28] M. K. McQuain, K. Seale, J. Peek, T. S. Fisher, S. Levy, M. A. Stremler & F. Haselton, "Chaotic mixer improves microarray hybridization," *Anal. Biochem*, **325**, 215 (2004).

[29] D. K. Schaffer, "Polymeric Microfluidic Components for Improved Microarray DNA Hybridization," *Graduate School of Vanderbilt University*, *Mechanical Engineering Master's Thesis* (2003).

[30] D. F. Young, B. R. Munson, T. H. Okiishi, "A Brief Introduction to Fluid Mechanics," *John Wiley & Sons, Inc.*, **2nd edition** (2001).

[31] H. Aref, "The development of chaotic advection," *Phys. Fluids* **14**, 1315-1325 (2002).

[32] E. N. Lorenz, "Deterministic nonperiodic flow," *J. Atmos. Sci.* **20**, 130 (1963).

[33] H. Aref, "An idealized model of stirring," *Woods Hole Oceanographic Institution Technical Report WHOI-82-45* pp.188-189 (1982).

[34] S. W. Jones & H. Aref, "Chaotic advection in pulsed source-sink systems," *Phys. Fluids* **31**, 469-485 (1988).

[35] J. Evans, D. Liepmann & A. P. Pisano, "Planar laminar mixer," *In Proc. IEEE Int. Workshop Micro Electro Mech. Sys., Nagoya, Japan, Jan. 26-30*, pp. 96-101 (1997).

[36] M. A. Stremler & B. A. Cola, "Chaotic Advection and Mixing in Pulsed Source-Sink Systems," *XXI ICTAM, Warsaw, Poland, Aug. 15-21*, (2004).